Acta Materialia 305 (2026) 121829

Contents lists available at ScienceDirect

Acta Materialia

journal homepage: www.elsevier.com/locate/actamat

Full length article

# Solvent-enriched interface enables ductility in an ultrastrong alloy

Ting Liu [a], Yunzhu Shi [a,*], Liuliu Han [b,*], Fei Zhang [c], Wei Chen [d], Hongyuan Wan [d], Chao Ma [a], Alexander Schökel [e], Yan Ma [f], Shaolou Wei [b], Claudio Pistidda [g], Zhifeng Lei [a,*], Zhaoping Lu [h,*]

[a] College of Materials Science and Engineering, Hunan University, Changsha 410082, China
[b] Department of Microstructure Physics and Alloy Design, Max Planck Institute for Sustainable Materials, 40237 Düsseldorf, Germany
[c] Institute of High Energy Physics, Chinese Academy of Sciences, Beijing, 100049, China
[d] Science and Technology on Power Beam Processes Laboratory, AVIC Manufacturing Technology Institute, Beijing, 100024, China
[e] Deutsches Elektronen-Synchrotron DESY, Notkestr. 85, 22607 Hamburg, Germany
[f] Department of Materials Science and Engineering, Delft University of Technology, Mekelweg 2, 2628 CD, Delft, the Netherlands
[g] Department of Materials Design, Institute of Hydrogen Technology, Helmholtz-Zentrum hereon GmbH, 21502 Geesthacht, Germany
[h] Beijing Advanced Innovation Center for Materials Genome Engineering, State Key Laboratory for Advanced Metals and Materials, University of Science and Technology Beijing, Beijing, 100083, China

ARTICLE INFO

*Keywords:*
Austenitic alloy
Low-angle grain boundaries
Solvent enrichment
Strength–ductility synergy

ABSTRACT

In metals and alloys, solute segregation at grain boundaries typically undermines cohesion and ductility. Here, we overturn this paradigm by showing that solvent Fe atoms can preferentially enrich low-angle grain boundaries (LAGBs) in a ferrous alloy, dramatically enhancing ductility. Cold rolling and aging generate coherent nanoprecipitates, a high dislocation density, and abundant LAGBs in an austenitic matrix, yielding an ultrahigh tensile yield strength of ~ 1.74 GPa. Moreover, the solvent Fe enrichment at LAGBs lowers local stacking fault energy and activates austenite-to-martensite transformation under load. This transformation-induced plasticity effect stabilizes plastic flow, enabling a uniform elongation of ~ 26.2 % despite the alloy's exceptional strength. Our findings challenge conventional views of segregation and offer a new design strategy for ultra-strong, highly ductile alloys.

## 1. Introduction

Alloys typically comprise a solvent element alongside several solute elements [1]. Variations in physical and chemical properties among these elements often result in non-uniform distribution [2], with a tendency for elements to segregate toward defect sites, particularly at interfaces such as grain boundaries that are prevalent in alloys. Solute atoms, present in lower concentrations and inducing greater lattice distortion than solvent atoms, have strong thermodynamic and kinetic incentives to segregate at grain boundaries [3–5].

Solute segregation at grain boundaries significantly impacts the microstructure and mechanical properties of alloys by altering the thermodynamic and kinetic behavior of grain boundaries [6–8]. For instance, solute segregation reduces grain boundary energy, capillary driving forces, and grain boundary mobility [9,10], which retards grain growth, stabilizing small grain sizes and increasing alloy strength in line with the Hall-Petch relationship [11–13]. However, this segregation often weakens cohesion, causing alloy embrittlement. In Mo alloys, oxygen segregation at grain boundaries increases the volume of polyhedron sites and reduces charge density among adjacent Mo atoms, weakening Mo-Mo bonds and disrupting grain boundary cohesion, thereby increasing the tendency for intergranular cleavage [14]. Similarly, in Al alloys, Mg segregation at grain boundaries causes expansion and charge density depletion, leading to significant grain boundary embrittlement [15]. Thus, while solute segregation at grain boundaries can improve alloy strength, it often compromises ductility [16]. The segregation of solute element B at grain boundaries is one of the few known strategies to improve alloy ductility, provided that the B concentration is maintained below its solubility limit in the matrix to avoid the formation of brittle borides. These borides can serve as sites for crack initiation and lead to catastrophic intergranular fracture [17].

The classical view that only solute elements exhibit pronounced grain boundary segregation has recently been challenged by both theoretical and experimental advances. For instance, Calderon et al.

* Corresponding authors.
*E-mail addresses:* yzshi@hnu.edu.cn (Y. Shi), l.han@mpie.de (L. Han), zflei@hnu.edu.cn (Z. Lei), luzp@ustb.edu.cn (Z. Lu).

https://doi.org/10.1016/j.actamat.2025.121829
Received 5 August 2025; Received in revised form 15 November 2025; Accepted 14 December 2025
Available online 15 December 2025

demonstrated a reversible solvent segregation transition in Au–Pt alloys, where Au—the solvent—was shown to enrich at grain boundaries following high-temperature annealing, driven by its lower intrinsic boundary energy relative to Pt [18]. This finding provided direct experimental evidence that solvent enrichment can, under certain conditions, dominate interface chemistry. More recently, Petrazoller et al. developed an elastic dipole model to predict segregation energy spectra at low-angle grain boundaries (LAGBs) [19]. Their analysis revealed that the coupling between atomic size misfit and the strain field of dislocation arrays generates energetically favorable segregation sites. Together, these advances establish a new theoretical foundation for understanding interface chemistry and open new opportunities for alloy design through controlled solvent and solute partitioning.

Here, we present a counterintuitive phenomenon in the Fe-33Ni-6Al-1.5Ta-1.5Ti-0.2C-0.05B (at. %) alloy, where solvent element Fe, rather than the expected solute elements, preferentially enriches at LAGBs with misorientation angles ranging from 2° to 15°. This solvent enrichment, coupled with a high density of coherent nanoprecipitates and dislocations, contributes to an exceptional tensile yield strength of ~ 1.74 GPa. Importantly, the solvent enrichment at LAGBs lowers the stacking fault energy in these areas, which promotes martensitic transformation. As a result, the alloy demonstrates an outstanding uniform elongation of ~ 26.2 %. These findings challenge conventional views of grain boundary segregation and open new avenues for designing high-strength, high-ductility alloys.

## 2. Materials and methods

### 2.1. Materials preparation

The alloy composition was optimized through systematic variation of Al content and the (Ta + Ti) content to balance strength and ductility (**Fig. S1**). The final composition, Fe-33Ni-6Al-1.5Ta-1.5Ti-0.2C-0.05B (at. %), was identified as the optimum formulation. The ferrous alloy was synthesized by arc-melting high-purity elemental metals (≥ 99.95 wt. %) along with carbon and boron (99.99 wt. %) under a Ti-gettered, high-purity argon atmosphere. To achieve chemical homogeneity, the ingots were remelted at least eight times before being drop-cast into a water-cooled copper mold with dimensions of 10 × 10 × 80 $mm^3$. The as-cast ingots underwent homogenization at 1200 °C for 2 h, yielding the solution-treated (ST) alloy. Subsequently, the homogenized alloys were cold-rolled to achieve a thickness reduction of ~ 90 %, forming the cold-rolled (CR) alloy. Aging treatments were then performed at 725 °C for 4 h to obtain the cold-rolled and aged (CRA) alloy. For comparison, an additional set of cold-rolled alloys was annealed at 1050 °C for 10 min, followed by aging at 725 °C for 4 h, producing the cold-rolled, annealed, and aged (CRAA) alloy. All thermal treatments were completed with water quenching to retain microstructural features.

### 2.2. Mechanical characterization

Dog-bone-shaped tensile samples with a 10 mm gauge length and 2 × 1 $mm^2$ cross-sectional area were prepared by electrical discharge machining. Before testing, all specimens were finally polished to a 2000-grit finish using SiC paper. Uniaxial tensile tests were conducted at ambient temperature on a Shimadzu AGS-X-50 kN universal testing machine, with a nominal strain rate of 1 × $10^{-3}$ $s^{-1}$. For each alloy condition, at least five samples were tested to ensure reproducibility and statistical accuracy.

### 2.3. Scanning electron microscopy (SEM)

Microstructural and morphological analyses were performed using a MIRA3 LMU scanning electron microscope (SEM, TESCAN company) operated at 20 kV at Hunan Nano Micro New Materials Technology Co., Ltd. Electron back-scattering diffraction (EBSD) mapping was conducted on a Zeiss Gemini 300 microscope equipped with an Oxford Symmetry detector at 15 kV, employing a 0.04 μm step size. Before imaging, specimens were prepared by grinding with 2000-grit SiC paper followed by mechanical polishing on a metallographic polishing machine (LMD-2C) to achieve a high-quality surface finish.

### 2.4. Transmission electron microscopy (TEM)

Detailed microstructure characterization and microstructural evolution at various stages of deformation were conducted using a transmission electron microscope (TEM, FEI Talos F200X) operated at 200 kV. Aberration-corrected scanning transmission electron microscopy (STEM, Thermo Scientific Themis Z in Analytical Instrumentation Center of Hunan University), equipped with a four-quadrant ChemiSTEM EDS system, was employed at 300 kV. TEM specimens were initially polished to a thickness of 50 μm, followed by twin-jet electropolishing in a solution of 90 % ethanol and 10 % perchloric acid (vol. %) at −25 °C with an applied voltage of 20 V. For aberration-corrected STEM, specimens were prepared using a Helios 5 CX dual-beam focused ion beam (FIB) system to achieve site-specific thinning.

### 2.5. Atom probe tomography (APT)

APT analyses were performed on a Cameca LEAP 5000XR instrument under ultrahigh vacuum conditions (approximately 2.5 × $10^{-11}$ torr). Measurements were carried out at 60 K, with a pulse frequency of 120 kHz and pulse energy of 40 pJ. Specimens for APT were prepared using a dual-beam FEI Helios 600i focused ion beam (FIB) system. Data reconstruction and analysis were completed using AP Suite software (v6.1).

### 2.6. Synchrotron X-ray diffraction (SXRD)

The phase compositions of the alloys were examined using SXRD at beamline 4W2 of the Beijing Synchrotron Radiation Facility (BSRF). A monochromatic X-ray diffraction beam with an energy of 60 keV (wavelength of 0.2061 Å) was employed; the detector position and orientation were calibrated with a $CeO_2$ standard. Two-dimensional (2D) diffraction patterns were acquired using a Pilatus3 × 2 M detector. The 2D images were integrated into one-dimensional (1D) XRD patterns along azimuths from 3° to 15° using Dioptas software [20]. Rietveld refinement was performed with GSAS-II software [21]. *In-situ* SXRD experiments were conducted at the Powder Diffraction and Total Scattering Beamline P02.1 of PETRA III at Deutsches Elektronen-Synchrotron (DESY) in Hamburg, Germany [22]. The beamline was operated at a fixed energy of 60 keV, providing a monochromatic X-ray with a wavelength of ~ 0.20738 Å. A Kammrath & Weiss stress rig with a maximum load of 5 kN was placed between the incident beam and the 2D detector to perform the tensile deformation. Sub-sized tensile samples (gauge length 12 mm, width 2 mm, thickness ~ 1 mm) were tested at room temperature with an initial strain rate of ~ 1 × $10^{-3}$. The sample-to-detector distance was approximately 1 m, with the incident beam size set to 0.6 mm × 0.6 mm. Calibration procedures were executed using a $LaB_6$ standard to ascertain the detector distance and instrument broadening. During tensile testing, 2D diffraction patterns were collected every 5 s using a fast area detector (Varex XRpad 4343CT, 2880 × 2880 pixels). These 2D Debye-Scherrer diffraction images were integrated into 1D patterns using GSAS-II software [23], with the phase evolution during tensile deformation analyzed by segmenting the 2D images into 5° sectors along the axial direction (azimuth angle 85°–95°).

## 3. Results

### 3.1. Solvent-enrichment-driven alloy design

We engineered an austenitic ferrous alloy that combines exceptional

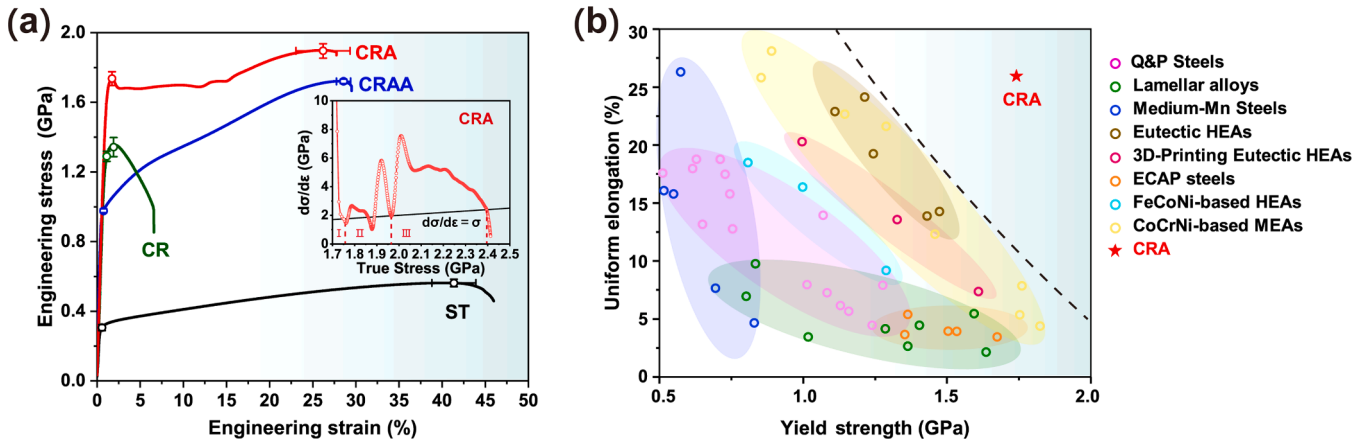


**Fig. 1. Mechanical properties. (a)** Room-temperature tensile engineering stress-strain curves of ST, CR, CRAA, and CRA alloys. The CRA alloy demonstrates an extraordinary combination of ultra-high yield strength and exceptional ductility. The inset displays the work-hardening rate and true stress-strain curves of the CRA alloy. The inset shows the Kocks-Mecking plot (work-hardening rate, θ versus true stress, σ) for the CRA alloy, revealing its distinctive multi-stage hardening behavior. **(b)** Comparison of uniform elongation versus yield strength of the CRA alloy with various other alloys, including quench and partition steels (Q&P steels) [24–28], lamellar alloys [29–31], medium-Mn steels [32,33], eutectic high-entropy alloys (HEAs) [34,35], 3D-printing eutectic HEAs [36,37], equal channel angular pressing (ECAP) steels [38,39], FeCoNi-based HEAs [40–42], and CoCrNi-based medium-entropy alloys (MEAs) [43–46].

strength with outstanding ductility by uniting targeted chemistry and controlled processing to drive solvent enrichment at grain boundaries. Starting from Fe-33Ni-6Al-1.5Ta-1.5Ti-0.2C-0.05B, we first selected an austenitic matrix to ensure excellent inherent deformability and high solute solubility. To impart exceptional yield strength, we incorporated Ni, Al, Ta, and Ti as the primary elements for forming coherent $L1_2$ nanoprecipitates during subsequent heat treatment, while minor C and B additions were included to refine grain boundary chemistry and stability. The processing route begins with a solution treatment at elevated temperature, dissolving solute elements into a homogeneous austenite phase. Immediately following this, heavy cold rolling imposes a high density of dislocations and an abundance of LAGBs, deliberately introducing a three-dimensional network of rapid diffusion pathways. These defects serve as highways for Fe atoms, dramatically lowering their diffusion barrier compared to the undisturbed lattice. Next, the alloy undergoes an intermediate-temperature aging treatment. During this step, the $L1_2$ nanoprecipitates nucleate and grow coherently within the austenite. Simultaneously, the high defect density created by cold rolling channels Fe solvent atoms toward the LAGBs, resulting in local enrichment. This dual strategy—composition engineering for precipitation hardening, combined with defect engineering to drive solvent enrichment—is essential to achieving the unprecedented combination of ultra-high strength and high ductility in this ferrous alloy.

### 3.2. Tensile properties

For clarity, we refer to the solution-treated alloy as ST and the cold-rolled alloy as CR. The alloy subjected to recrystallization annealing before aging is termed CRAA, while the alloy aged directly after cold rolling is designated CRA. Fig. 1**a** presents the room-temperature tensile engineering stress-strain curves for these alloys. The ST alloy demonstrates a tensile yield strength of 306 ± 18 MPa with a uniform elongation of 41.4 % ± 5.6 %. In contrast, while the CR alloy achieves a tensile yield strength of 1290 ± 29 MPa, its uniform elongation is markedly reduced to 1.9 % ± 0.1 %. The CRA alloy, however, exhibits an impressive tensile yield strength of 1737 ± 39 MPa coupled with a uniform elongation of 26.2 % ± 3.1 %, outperforming the CR alloy in both metrics. Furthermore, even compared to its fully recrystallized counterpart, CRAA, the CRA alloy nearly doubles the yield strength while maintaining a comparable uniform elongation. Such a marked increase in yield strength through cold rolling and aging, without compromising ductility, is exceedingly rare. The Kocks-Mecking (K-M) plot (**inset in** Fig. 1**a**) reveals a distinctive multi-stage work-hardening response in the CRA alloy, indicating the activation of complex deformation mechanisms, which are discussed in detail in subsequent sections. Fig. 1**b** compares the yield strength and uniform elongation of CRA with other typical alloys. Remarkably, CRA exhibits an unprecedented combination of ultra-high yield strength and superior ductility.

### 3.3. Microstructure characterization

To elucidate the mechanisms behind the strengthening and ductilization of the CRA alloy, we conducted a detailed microstructural analysis. Fig. 2**a** presents synchrotron high-energy X-ray diffraction (SXRD) patterns for the ST, CR, CRAA, and CRA alloys. Both the ST and CR alloys primarily consist of face-centered cubic (FCC) austenite. However, the CRAA and CRA alloys predominantly exhibit both FCC and $L1_2$ phases. In the CRA alloy, the lattice parameters for FCC austenite and $L1_2$ phase are 3.6167 ± 0.0009 Å and 3.6224 ± 0.0023 Å, respectively, resulting in a lattice misfit of 0.16 % (**Fig. S2**). Additionally, all these alloys exhibit small amounts of (Ta, Ti)C carbides. Scanning electron micrographs further reveal that these finely dispersed carbides constitute a small fraction (~ 3 %) of the microstructure in the CRA alloy (**Fig. S3**). Their direct influence as heterogeneous nucleation sites for $L1_2$ precipitates or as major pinning agents for dislocations and grain boundaries is expected to be minor. Electron backscatter diffraction (EBSD) analysis reveals that the CRA alloy contains a high fraction of LAGBs (~ 95.7 %) (**Fig. S4**). In contrast, the CRAA alloy exhibits a fully recrystallized microstructure after annealing at 1050 °C, characterized by a single FCC phase, equiaxed grains (~ 28.8 μm), a distinct <101> texture, and uniformly low kernel average misorientation—all confirming the absence of deformation substructures (**Fig. S5**). Fig. 2**b** shows an aberration-corrected scanning transmission electron microscope high-angle annular dark field (STEM-HAADF) image of the CRA alloy, revealing high-density spherical nanoprecipitates (yellow arrows) and grain boundaries (white arrows) within the austenite matrix. Further, selected area electron diffraction (SAED) analysis demonstrates that the nanoprecipitates are $L1_2$ phase, and the grain boundaries are LAGBs (Fig. 2**c**). A dark-field transmission electron microscopy (TEM) image further demonstrates the distribution of $L1_2$ nanoparticles, approximately 10 nm in size, within the matrix (Fig. 2**d**). A representative aberration-corrected STEM-HAADF micrograph shows a fully coherent interface between $L1_2$ nanoprecipitates and the FCC matrix (Fig. 2**e**). Fig. 2**f** displays a typical STEM-HAADF image and corresponding

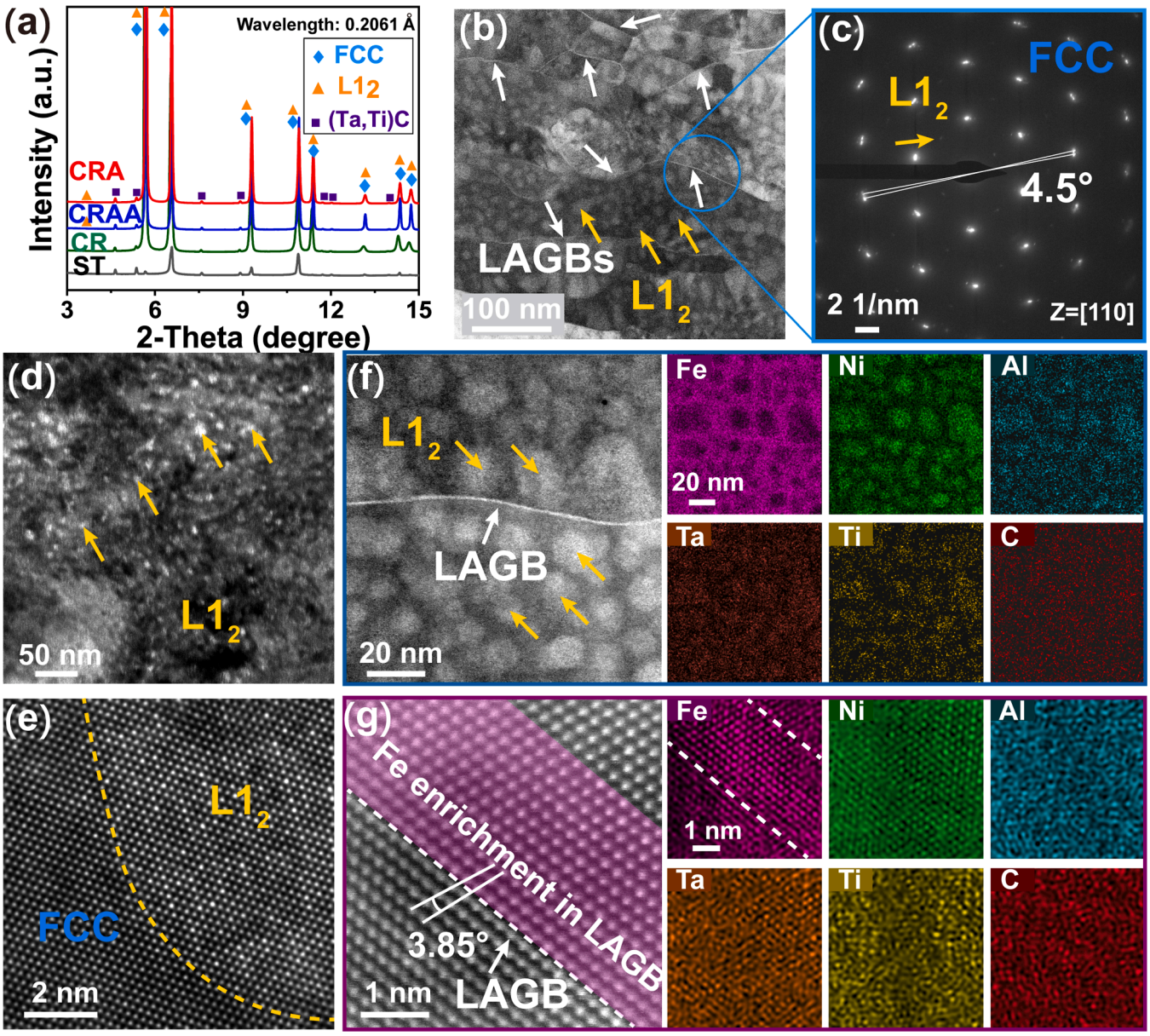


**Fig. 2. Microstructures. (a)** Synchrotron high-energy X-ray diffraction (SXRD) patterns of the ST, CR, CRAA, and CRA alloys. The ST and CR alloys primarily consist of face-centered cubic (FCC) austenite with a small amount of carbides, while the CRA and CRAA alloys predominantly contain FCC austenite and $L1_2$ phases. **(b)** Aberration-corrected scanning transmission electron microscopy high-angle annular dark field (STEM-HAADF) image of the CRA alloy, showing spherical $L1_2$ nanoprecipitates (yellow arrows) and numerous low-angle grain boundaries (LAGBs) (white arrows) in the matrix. **(c)** Selected area electron diffraction (SAED) pattern from the blue circle in **b**, displaying the FCC austenite matrix, $L1_2$ precipitates, and LAGBs (misorientation angle 4.5°) along the $[110]_{FCC}$ zone axis. **(d)** Dark-field transmission electron microscopy (TEM) image of the $L1_2$ precipitates using a superlattice reflection. **(e)** Aberration-corrected STEM-HAADF image highlighting the interfacial coherency between $L1_2$ precipitates and the FCC matrix. **(f)** STEM image and corresponding STEM energy-dispersive X-ray spectroscopy (EDS) maps, showing $L1_2$ precipitates and an LAGB in the CRA alloy. **(g)** Atomic-resolution STEM-HAADF image and EDS maps of an LAGB (misorientation angle 3.85°), with Fe enrichment observed at the LAGB.

energy-dispersive X-ray spectroscopy (EDS) mapping of the CRA alloy. The analysis reveals that Ni, Al, Ta, and Ti are concentrated in the nanoprecipitates, while Fe predominantly remains in the matrix, with a slight tendency to accumulate at the LAGBs. To further explore Fe enrichment, atomic resolution STEM-HAADF imaging and EDS mapping were performed at the LAGBs (Fig. 2**g**), revealing a thin Fe-enriched layer, approximately 2 nm thick.

The localized chemistry of the CRA alloy at the near-atomic scale was investigated by atom probe tomography (APT), as shown in Figs. 3**a–d**. A three-dimensional APT tip with a thickness of 20 nm visualized the different chemistries between the $L1_2$ nanoparticles and the FCC matrix (Fig. 3**a**). The volume fraction and number density of the uniformly distributed $L1_2$ nanoparticles were determined to be 23.9 % and 3.5 × $10^{23}$ $m^{-3}$, respectively, based on isocomposition surfaces containing 50 at. % Ni (**Fig. S6**). The corresponding proximity histograms using the same isocomposition surfaces, that is, 50 at. % Ni is shown in Fig. 3**b**. Across the $L1_2$-(FCC matrix + LAGBs) interfaces, Ni, Al, Ta, and Ti accumulate in the $L1_2$ nanoparticles, while Fe is enriched in the FCC matrix and LAGBs. It should also be noted that enrichment of Fe and depletion of Ni were observed in the LAGBs within the FCC matrix, as indicated by the black arrows in Fig. 3**a**. This is also confirmed by the density distribution map of Fe in the FCC matrix (Fig. 3**c**). Fig. 3**d** shows the corresponding one-dimensional elemental profiles computed along the cylinder in Fig. 3**a**. The Fe element concentration in the matrix is ~

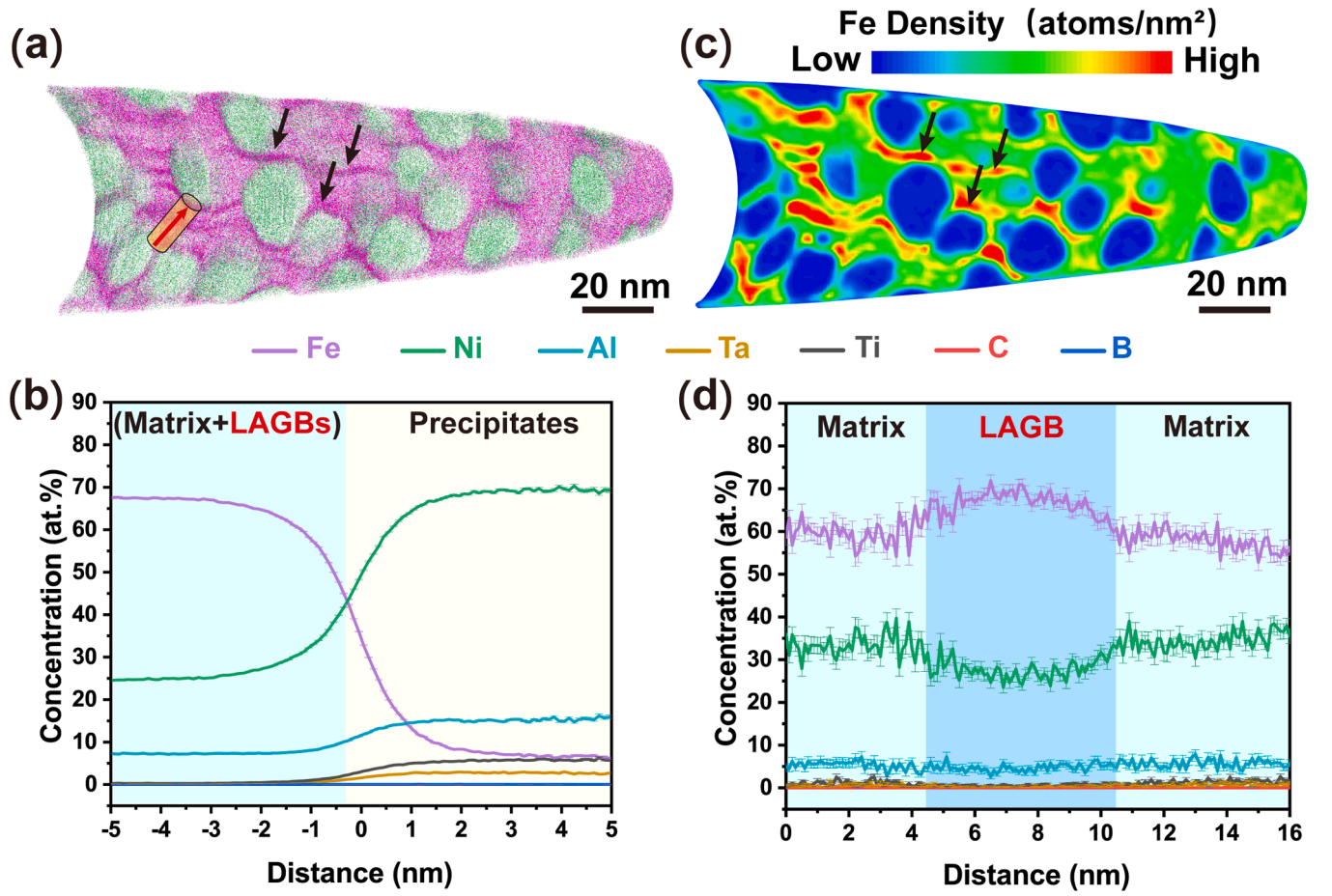


**Fig. 3. Atom probe tomography (APT) analysis of the CRA alloy. (a)** Three-dimensional atom probe tomography reconstruction of the CRA alloy specimen. The thickness of the three-dimensional APT tip is 20 nm. **(b)** Proximity histograms computed using 50 at. % Ni showing the concentration across the FCC matrix and $L1_2$ nanoprecipitates. **(c)** The corresponding density map shows the enrichment of Fe in the LAGBs. **(d)** One-dimensional concentration profiles are perpendicular to the interfaces of the LAGBs.

60 at. %, while the Fe elemental enrichment concentration at the LAGB reaches up to ~ 70 at. %. The detailed compositions of the FCC matrix, $L1_2$ nanoprecipitates, and LAGBs are provided in **Table S1**.

### 3.4. *Deformation mechanism*

To explore the plastic deformation behavior of the CRA alloy, we examined its microstructural evolution under loading. At 5 % strain, body-centered cubic (BCC) martensite with an estimated volume fraction of 5 % forms along the LAGBs within the austenite matrix (Fig. 4**a**). Concurrently, the matrix develops a dislocation cell structure, characterized by a high density of entangled dislocations, and several stacking faults (Figs. 4**b** and **c**). Interestingly, dislocations traverse the LAGBs (**Fig. S7**). Upon reaching 15 % strain, the volume fraction of BCC martensite increases substantially to about 10 %, with the martensite predominantly aligning along LAGBs (Fig. 4**d**). A dark field TEM image reveals the presence of BCC martensite (Fig. 4**e**), with the corresponding SAED pattern demonstrating a Kurdjumov-Sachs (K-S) orientation relationship with the austenite matrix, specifically $\{110\}_{BCC}//\{111\}_{FCC}$ and $<-111>_{BCC}//<011>_{FCC}$ (inset in Fig. 4**e**). This indicates an indirect martensitic transformation through the sequence FCC austenite→hexagonal closed-packed (HCP) martensite→BCC martensite [47]. Stacking faults, aligned parallel to each other, and cutting through $L1_2$ nanoparticles, are also observed in the matrix (Fig. 4**f**). After the fracture, the volume fraction of BCC martensite increases further to 40 % (Fig. 4**g**). A dark field TEM image illustrates the development of BCC martensite laths (Fig. 4**h**). The SAED pattern from these laths, alongside the corresponding dark field TEM image, confirms the persistence of $L1_2$ nanoparticles within the martensite (Fig. 4**i**). This finding underscores that, despite the martensitic transformation of the austenite, the $L1_2$ nanoparticles remain intact. Thus, in the CRA alloy, martensitic transformation plays a dominant role in plastic deformation, with martensite primarily forming along LAGBs (Fig. 4**j**).

To further elucidate the deformation mechanism of the CRA alloy, we conducted *in-situ* SXRD experiments during tensile loading. Fig. 5**a** presents the integrated diffraction patterns recorded along the loading direction. As strain increases, additional diffraction peaks corresponding to BCC and HCP martensites emerge at approximately 5.4 % strain, signifying an indirect martensitic transformation pathway (FCC austenite→HCP martensite→BCC martensite). The diffraction intensity of BCC martensite further intensifies with continued straining (see the inset in Fig. 5**a**). Phase quantification via Rietveld refinement, based on the *in-situ* SXRD data (**Fig. S8**), tracks the evolution of BCC and HCP martensite volume fractions as a function of applied engineering strain (Fig. 5**b**). Notably, the BCC martensite volume fraction increases rapidly during deformation, reaching approximately 40 % at fracture, while the HCP martensite fraction increases more gradually. These findings indicate that indirect martensitic transformation primarily drives the plastic deformation of the austenitic matrix in the CRA alloy.

In contrast, martensitic transformation also plays a crucial role in shaping the plastic deformation behavior of the CRAA alloy (Fig. 6). Deformation proceeds through a sequence of dislocation motion, stacking fault formation, and strain-induced phase transformation. At 5 % strain, dislocations and stacking faults appear, indicating that early-

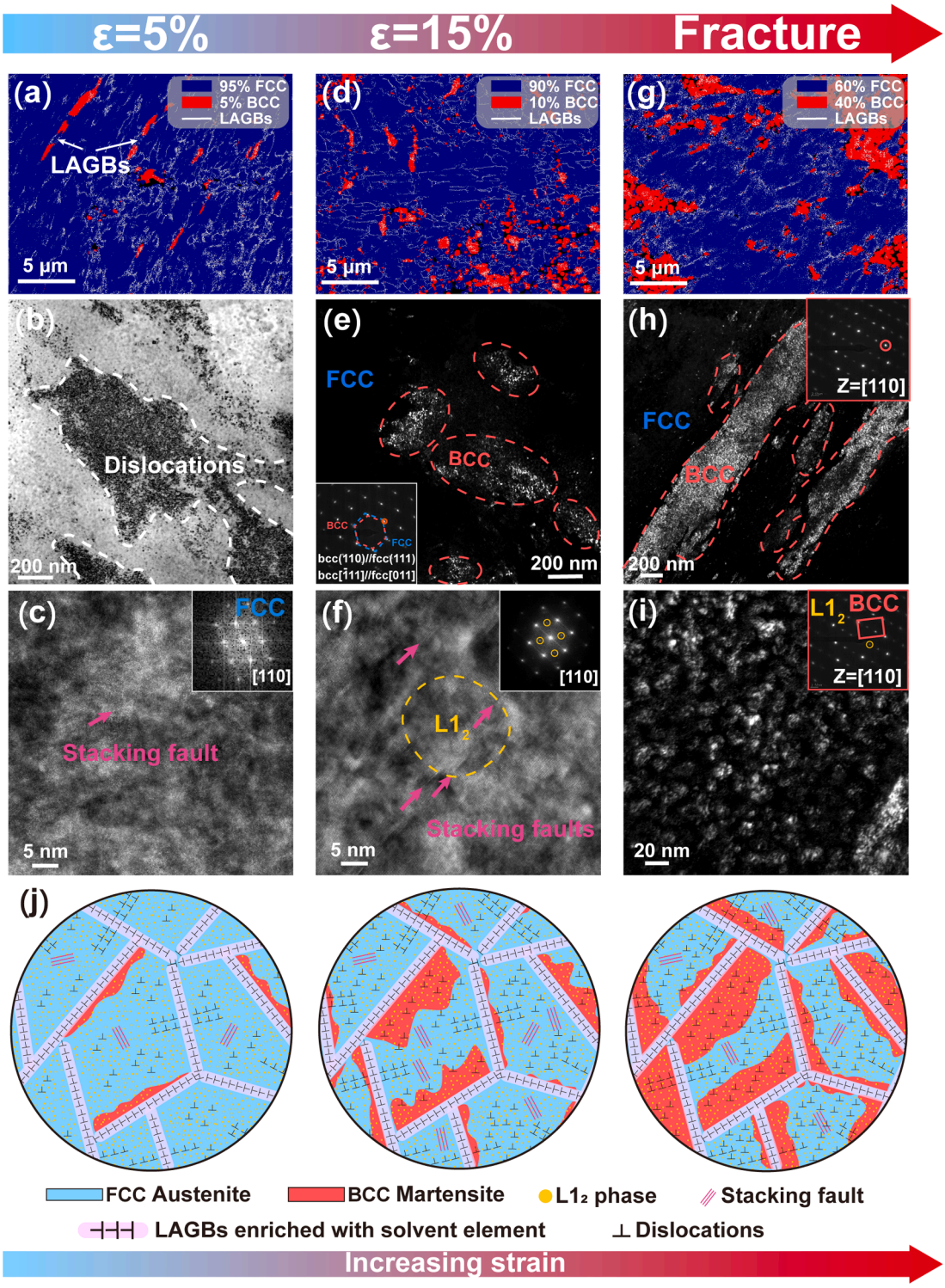


**Fig. 4. Deformation behavior of the CRA alloy. (a)** Electron back-scattering diffraction (EBSD) phase map showing the onset of the FCC austenite to BCC martensite transformation along the LAGBs (white arrows) at 5 % strain. **(b)** Bright-field TEM image of the austenite matrix with a high density of dislocations at 5 % strain. **(c)** High-resolution TEM image revealing the activation of planar stacking faults (purple arrows) within the austenite matrix at 5 % strain. Inset: Fast Fourier transform (FFT) pattern corresponding to the austenite matrix. **(d)** EBSD phase map showing the progression of martensite formation (10 % martensite) near LAGBs at 15 % strain. **(e)** Dark-field TEM image of martensite, acquired using the {110} BCC reflection at the $[110]_{FCC}$ zone axis. The inset SAED pattern confirms the Kurdjumov-Sachs orientation relationship (K-S OR) between the austenite and martensite. **(f)** High-resolution TEM image showing the formation of multiple stacking faults (purple arrows). $L1_2$ precipitates are sheared by stacking faults. Inset: SAED pattern of the austenitic matrix along the $[110]_{FCC}$ zone axis. **(g)** EBSD phase map indicating the formation of 40 % martensite near LAGBs at fracture. **(h)** Dark-field TEM image of martensite, using the {200} lattice reflection (red circle in inset) of martensite at the $[110]_{BCC}$ zone axis, illustrating a substantial martensitic transformation of the austenite matrix. **(i)** Dark-field TEM image of $L1_2$ precipitates, using the {100} superlattice reflection (yellow circle in inset) at the $[110]_{BCC}$ zone axis, showing $L1_2$ precipitates in the martensitic phase. **(j)** Schematic illustration of the deformation mechanism in the CRA alloy.

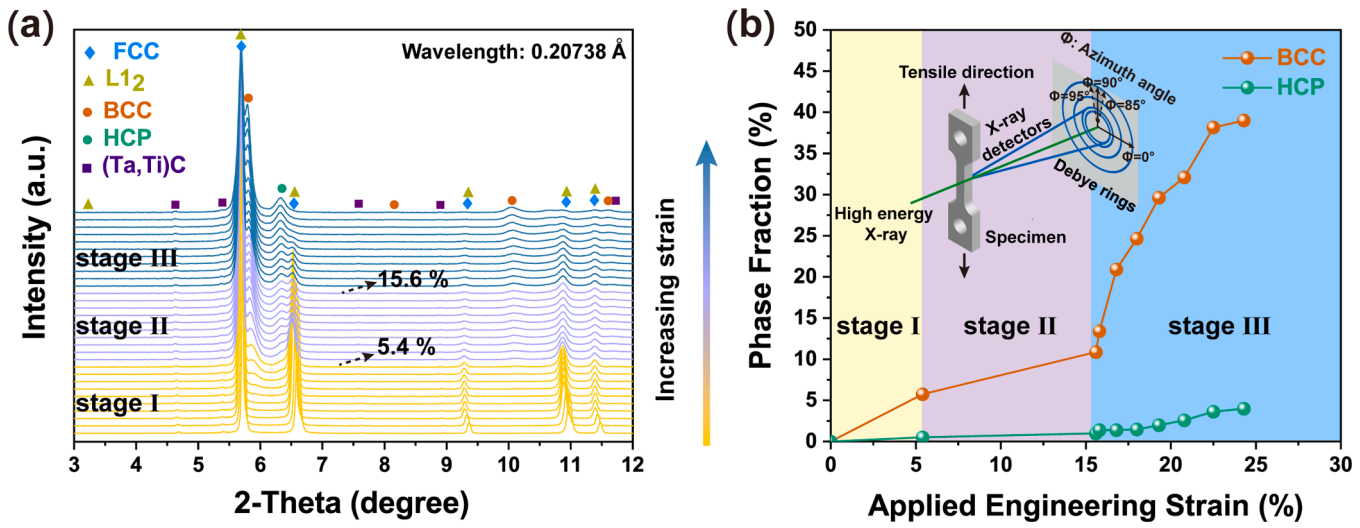


**Fig. 5.** ***In-situ*** **synchrotron X-ray diffraction measurements of the CRA alloy. (a)** One-dimensional diffraction patterns were integrated along the tensile direction at various stages of deformation. Stage I corresponds to the state before the martensitic transformation. Stage II marks the initiation of the martensitic transformation of the FCC austenitic matrix. Stage III corresponds to the significant martensitic transformation occurring. **(b)** Volume fraction of HCP and BCC martensites as a function of applied engineering strain, illustrating the evolution of phase fractions during deformation in the CRA alloy. Inset: Schematic illustration of the *in-situ* X-ray diffraction measurements, with the integrating sectors indicated.

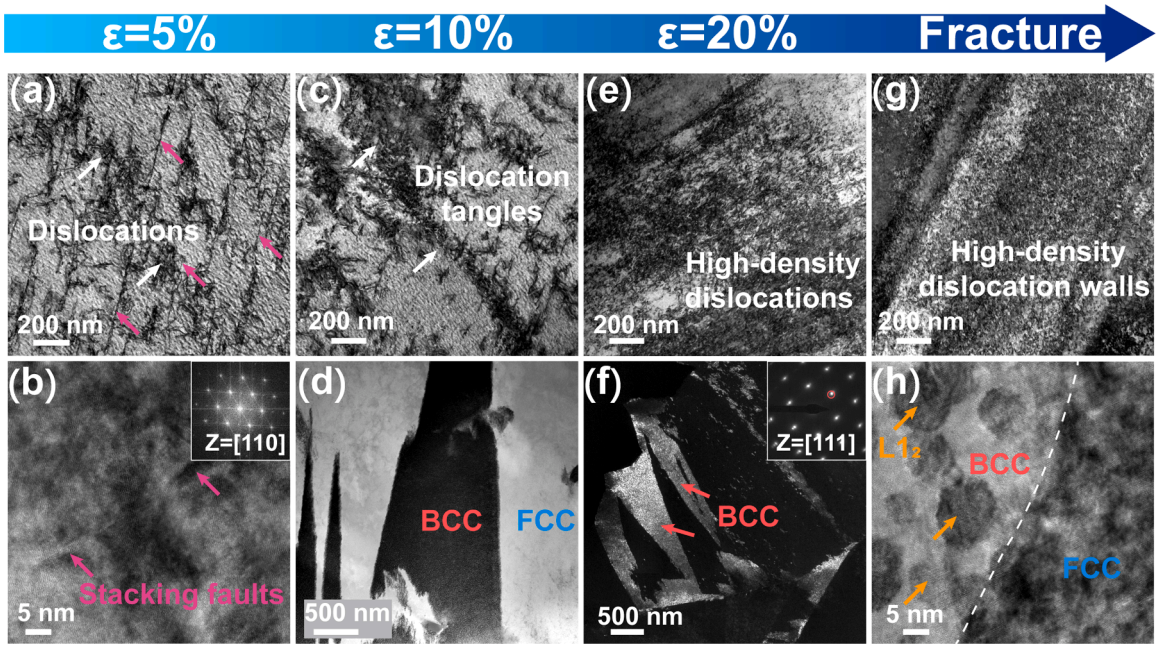


**Fig. 6. Deformation behaviors of CRAA alloy. (a)** Bright-field TEM image of CRAA alloy at 5 % strain. (**b**) STEM-HAADF image of CRAA alloy at 5 % strain. (**c**) Bright-field TEM image of CRAA alloy at 10 % strain. (**d**) The FCC austenite to BCC martensitic transformation starts to occur at 10 % deformation. (**e**) Bright-field TEM image of CRAA alloy at 20 % strain. (**f**) Dark-field TEM image of BCC martensite using the {110} lattice reflection (red circles in inset) at the $[111]_{BCC}$ zone axis. (**g**) Bright-field TEM image of CRAA alloy at fracture. (**h**) STEM-HAADF image of CRA alloy at fracture.

stage deformation is driven by dislocation glide and planar faulting (Figs. 6**a** and 6**b**). As strain increases to 10 %, dislocations begin to entangle, and a phase transformation from FCC austenite to BCC martensite initiates (Figs. 6**c** and 6**d**). By 20 % strain, dislocation density rises sharply, and widespread martensitic transformation occurs throughout the matrix (Figs. 6**e** and **f**). At fracture, bright-field TEM reveals dense dislocation walls, highlighting severe plastic deformation (Fig. 6**g**). Notably, $L1_2$ precipitates remain intact within the BCC martensite, as shown in the STEM-HAADF image (Fig. 6**h**), confirming their stability during the transformation. These observations suggest that recrystallization has little influence on the alloy's deformation behavior.

### 3.5. *Solvent enrichment promoted martensitic transformation*

To clarify the influence of solvent Fe enrichment at LAGBs on the plastic deformation behavior of the CRA alloy, we investigated the phase stability of both the austenitic matrix and the enrichment nanolayers. The fact that a bulk alloy with a composition equivalent to the Fe-enriched LAGBs forms a martensitic (BCC) microstructure (**Fig. S9**) intuitively suggests a drastically reduced stability of the FCC phase in this composition compared to the austenitic matrix. To quantitatively

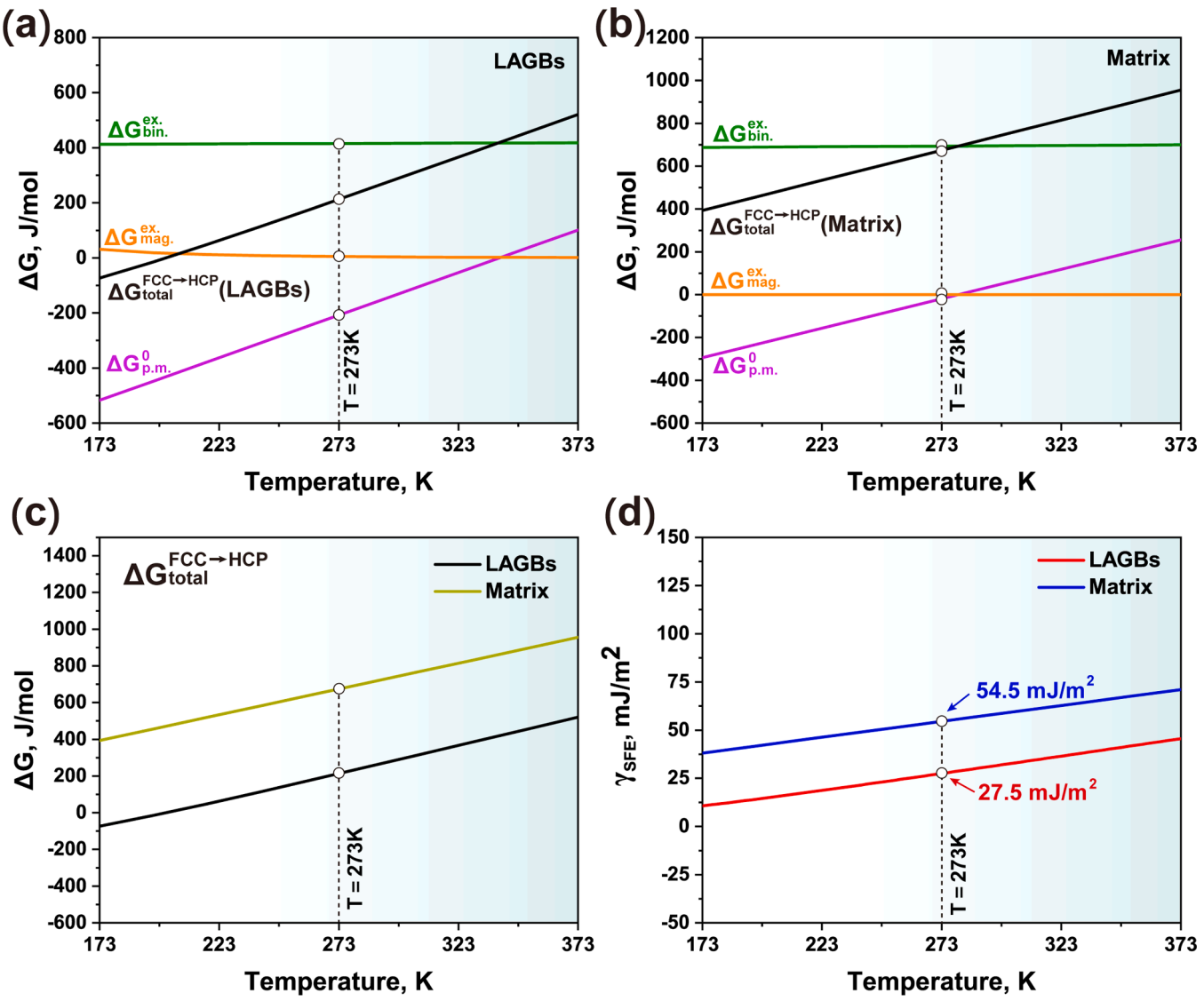


**Fig. 7. Thermodynamic calculation of the CRA alloy. (a, b)** Phase stability assessment using the sub-regular solution formalism for LAGBs and the FCC austenitic matrix. The term $\Delta G_{total}^{FCC\rightarrow HCP}$ denotes the total Gibbs free energy change for the FCC to HCP phase transformation. $\Delta G_{p.m.}^{o}$ represents the Gibbs free energy difference between the FCC and HCP phases in the pristine state, $\Delta G_{bin.}^{ex.}$ corresponds to the binary excess free energy, and $\Delta G_{mag.}^{ex.}$ refers to the magnetic contribution. **(c)**The total Gibbs free energy change $\Delta G_{E}^{FCC\rightarrow HCP}$ for LAGBs and the austenitic matrix. **(d)** Comparison of the intrinsic stacking fault energy of LAGBs and the austenitic matrix as a function of temperature.

confirm this and compare it with the matrix, direct experimental determination of the stacking fault energy (SFE) is precluded, as conventional techniques require a stable FCC structure. We therefore employed thermodynamic calculations to estimate the relative SFE variation between the LAGB and matrix regions. The compositional data obtained from APT for both regions were directly incorporated into these calculations. The SFEs were estimated using a thermodynamic model adapted from Olson and Cohen [48], which relates the SFE to the free energy difference between the FCC and HCP phases (**Note S1**). Figs. 7**a** and 7**b** present phase stability assessments of the matrix and LAGBs using subregular solution formalism. The Gibbs free energy difference between the FCC and HCP phases ($\Delta G_{total}^{FCC\rightarrow HCP}$) approaches zero at LAGBs near room temperature, whereas it remains significantly positive in the matrix, indicating reduced austenite stability at LAGBs. This is further corroborated by the temperature dependence of $\Delta G_{total}^{FCC\rightarrow HCP}$ in both regions (Fig. 7**c**). Additionally, at ambient temperature, the SFEs for the LAGBs and matrix are estimated to be 27.5 mJ/m$^2$ and 54.5 mJ/m$^2$, respectively (Fig. 7**d**). These results suggest that Fe enrichment at LAGBs reduces austenite stability, thereby promoting martensitic transformation during plastic deformation of the alloy.

## 4. Discussion

### 4.1. Formation of the solvent-enriched interface

In the CRA alloy, the enrichment of solvent Fe at LAGBs constitutes a key microstructural feature, achieved through a systematic exploration and optimization of the thermomechanical processing route (see **Note S2 and Fig. S10**). This section demonstrates that this phenomenon is fundamentally a thermodynamically driven process, the realization of which is kinetically facilitated by the specific thermomechanical processing route.

#### 4.1.1. Thermodynamic driving force for Fe segregation

The thermodynamic tendency for Fe to segregate to LAGBs originates from a reduction in chemical potential, which is governed by the system's Gibbs free energy under constant pressure and temperature [49].

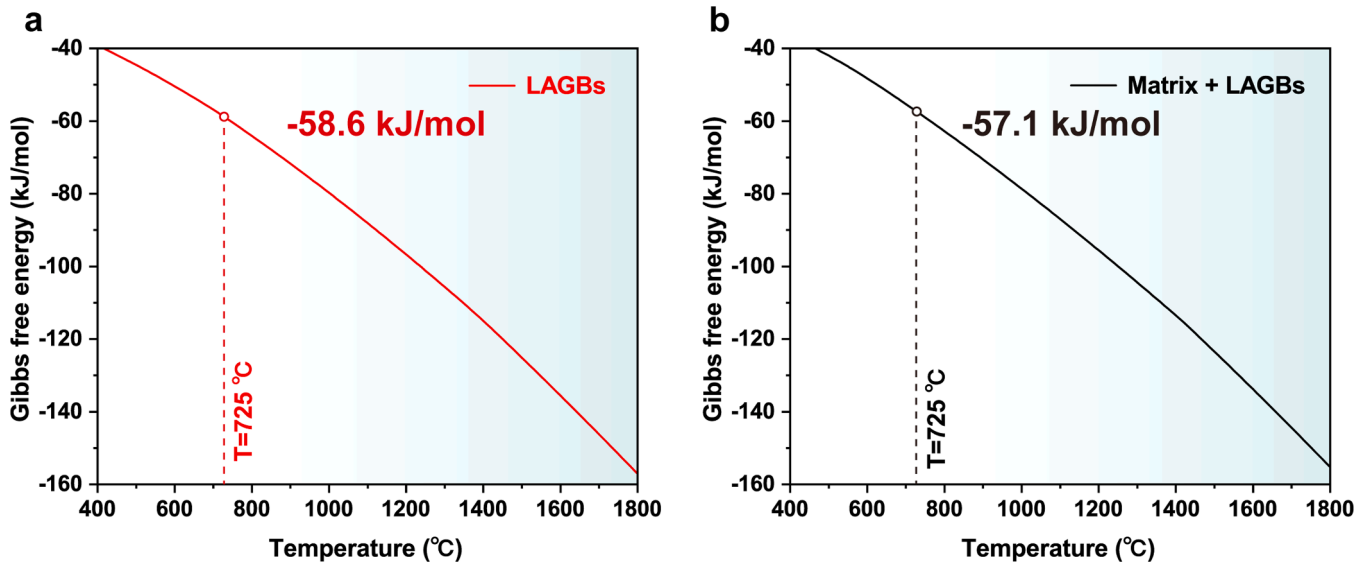


**Fig. 8. Temperature dependence of Gibbs free energy for LAGBs and matrix–boundary system.** At 725 °C, the Gibbs free energy of the Fe-enriched LAGBs is calculated as –58.6 kJ/mol, compared to –57.1 kJ/mol for the combined matrix and LAGB system. The lower free energy of the enriched boundaries indicates enhanced interfacial stability driven by Fe enrichment.

To evaluate the thermodynamic driving force for the observed LAGB chemistry, we compared the Gibbs free energy of two chemically defined systems derived from APT: the local Fe-enriched LAGB composition (LAGBs) and the bulk FCC matrix composition (Matrix + LAGBs). Gibbs free energies were calculated using Thermo-Calc (TCHEAT database) over 400–1800 °C, with the comparison reported at the aging temperature of 725 °C (Fig. 8). LAGB exhibits a lower Gibbs free energy than (Matrix + LAGBs), indicating a thermodynamic preference for the Fe-enriched LAGB composition.

To quantitatively assess the thermodynamic driving force for elemental segregation, the Gibbs free energy change of segregation ($\Delta G_{seg}$) for each element was calculated using the classical Langmuir-McLean isotherm [49]:

$$\frac{X_i^{GB}}{(1-X_i^{GB})} = \frac{X_i}{(1-X_i)} \exp\left(-\Delta G_{seg}/RT\right) \tag{1}$$

where $X_i^{GB}$ and $X_i$ are the concentration of element $i$ at the grain boundary and in the matrix, respectively, and $R$ is the gas constant. As shown in **Fig. S11**, Fe exhibits a negative segregation energy (−3.66 kJ/mol), confirming its thermodynamic preference for LAGB enrichment, while all other alloying elements (Ni, Al, Ta, Ti) have positive segregation energies, indicating the opposite tendency.

To present the effect normalized to grain-boundary area, we computed the interfacial excess of Fe ($\Gamma_{Fe}$) and the corresponding change in interfacial energy ($\Delta\gamma$) via the Gibbs adsorption approach [49,50]:

$$\Gamma_{Fe} = \frac{(X^{GB} - X^{Bulk})}{(V_m)} \cdot \delta \tag{2}$$

$$\Delta\gamma = \Gamma_{Fe} \cdot \left|\Delta G_{seg}^{Fe}\right| \tag{3}$$

Here $X^{GB}$ and $X^{Bulk}$ are the atomic fractions determined by APT, δ is the enrichment-layer thickness (from APT), $\Delta G_{seg}^{Fe} = -3.66$ kJ/mol and $V_m$ is the molar volume (from alloy density 7.972 g/cm$^3$ and mean atomic weight 56.7 g/mol). This yields $\Delta\gamma \sim -106$ mJ/m$^2$, indicating that Fe segregation lowers the grain-boundary energy by ~ 106 mJ/m$^2$. The normalized excess energy agrees with the Thermo-Calc Gibbs-energy comparison and the negative segregation energy, supporting the conclusion that Fe enrichment at LAGBs is thermodynamically spontaneous and significant in magnitude.

Thermo-Calc simulations provide a macroscopic view of the thermodynamic stability associated with Fe enrichment. At the atomic scale, recent theoretical insights help elucidate the underlying mechanisms. Petrazoller et al. introduced an elastic dipole model that predicts segregation energy spectra at LAGBs, demonstrating that the interaction between atomic size misfit and the strain field of a dislocation wall creates favorable segregation sites [19]. While our alloy system is considerably more complex than the binary systems examined in that study, the underlying principle remains applicable: atoms that relieve local elastic strain energy will preferentially segregate to regions of high strain.

In the CRA alloy, a dense network of edge dislocations forms LAGBs with significant elastic strain fields. The spatial correlation between Fe-enriched regions in the APT data (Fig. 3) and these boundaries suggests that segregation is at least partly driven by such elastic interactions. This defect-mediated mechanism is further corroborated by the crystallographic character of the interfaces. EBSD analysis confirms that the boundary network is overwhelmingly composed of random LAGBs, with special low-Σ coincident site lattice boundaries constituting <1.5 % of the total population (**Fig. S12**). The predominant Fe enrichment at these random LAGBs, rather than at specific crystallographic boundaries, demonstrates that the driving force for segregation originates from the local elastic strain and high defect density inherent to dislocation arrays. Although a full quantitative simulation using the elastic dipole approach is beyond the scope of the present work, the qualitative consistency between its physical predictions and our experimental observations strongly supports a defect-mediated, thermodynamically favorable segregation process that operates across different compositional complexities.

#### 4.1.2. *Kinetic pathways enabled by processing*

While thermodynamics defines the equilibrium state, its realization within practical time scales requires efficient kinetic pathways. In our CRA alloy, the cold-rolling and aging process ensures both the supply and transport of Fe atoms to LAGBs through two complementary mechanisms. The supply of Fe atoms is established through elemental partitioning. The distribution of elements is quantified by the partitioning coefficient [51]:

$$k_i = \frac{C_i^{L1_2}}{C_i^{FCC}} \tag{4}$$

**Table 1**
Elemental partitioning coefficient $k_i$.

| Elements | Fe | Ni | Al | Ta | Ti |
|---|---|---|---|---|---|
| $k_i$ | 0.099 | 2.789 | 2.116 | 15.028 | 20.610 |

**Table 2**
Calculated diffusion coefficients and diffusion activation energies for each element at 725 °C.

| Elements | Fe | Ni | Al | Ta | Ti |
|---|---|---|---|---|---|
| Intrinsic diffusion coefficient ($10^{-4}$ $m^2$/s) | 6.8 | 5.12 | 1 × $10^{-4}$ | 1.9 × $10^{-3}$ | 1.7 × $10^{-8}$ |
| Diffuse activation energy (kJ/mol) | 258.9 | 297.3 | 260 | 370.8 | 192.8 |
| Diffusion coefficient at 725 °C ($m^2$/s) | 1.81 × $10^{-17}$ | 1.32 × $10^{-18}$ | 2.3 × $10^{-18}$ | 6.89 × $10^{-27}$ | 1.32 × $10^{-18}$ |

Where $C_i^{L1_2}$ and $C_i^{FCC}$ represent the atomic fractions of element $i$ in the $L1_2$ and FCC phases, respectively. Accordingly, Fe preferentially partitions to the FCC matrix ($k_i < 1$), while Ni, Al, Ta, and Ti favor the $L1_2$ precipitates ($k_i > 1$) (Table 1). Consequently, Fe is preferentially retained in the FCC matrix, while Ni, Al, Ta, and Ti concentrate in the $L1_2$ precipitates.

In addition, LAGBs serve as fast diffusion pathways, promoting atomic accumulation. The self-diffusion coefficients for each element at 725 °C were calculated using the equation [52,53]:

$$D = D_0 \exp\left(-Q_D / RT\right) \tag{5}$$

Where $D$ is the diffusion coefficient, $D_0$ is the intrinsic diffusion coefficient and $Q_D$ is the activation energy for diffusion. Fe exhibits a higher diffusion coefficient than the solute Ni, Al, Ta, and Ti elements (Table 2), indicating a faster diffusion rate. As a result, Fe preferentially diffuses to the LAGBs, leading to its enrichment at these boundaries.

This finding was further supported by tracer diffusion coefficients calculated using the TCFE10 module of Thermo-Calc in combination with the MOBFE5 mobility database (**Fig. S13**). This method captures the complex solute–solute interactions in the concentrated alloy, yielding more realistic diffusivity values than handbook estimates. The results indicate that Al diffuses fastest, followed by Fe, while Ni, Ta, and Ti are markedly slower. Although Al exhibits the highest diffusivity, its strong partitioning into $L1_2$ precipitates limits its effective mobility at boundaries. In contrast, Fe, with its high diffusivity and weak affinity for precipitates, readily migrates toward LAGBs and accumulates there, underscoring the coupled thermodynamic and kinetic origins of solvent enrichment. This principle is further exemplified by other alloying elements: the interstitial carbon is effectively gettered by stable (Ta, Ti)C carbides, while boron's negligible concentration (0.05 at. %) precludes any significant segregation competition. Consequently, Fe emerges as the uniquely optimized element, combining high matrix solubility, superior mobility, and a strong thermodynamic driving force for boundary segregation.

Comparison between the CRA and CRAA samples provides definitive evidence that the observed Fe segregation is a thermodynamically driven phenomenon kinetically enabled by the defect structure. As shown in **Fig. S14**, the CRAA alloy, which underwent recrystallization annealing before aging and thus lacks the dense network of dislocations and LAGBs, exhibits no detectable Fe enrichment at grain boundaries. In contrast, the CRA alloy displays pronounced Fe segregation along LAGBs, consistent with a lower Gibbs free energy for the Fe-enriched configuration. These observations establish that the solvent segregation is not a transient kinetic artifact but a stable thermodynamic state that can only be realized when sufficient diffusion pathways are available. The formation of this solvent-enriched interface therefore reflects a synergistic interplay between thermodynamics, which defines the equilibrium configuration, and kinetics, which governs its accessibility.

It is important to note, however, that this "thermodynamically favored configuration" exists within the specific microstructural context of a metastable matrix containing a high density of nonequilibrium defects. The stability of this solvent-enriched state was further examined by prolonged aging at 725 °C for 48 h (see **Figs. S15 and S16**). Extended annealing results in pronounced microstructural coarsening and a marked reduction in Fe enrichment at LAGBs, accompanied by a severe loss in both yield strength and ductility. These results confirm that the solvent-enriched LAGB structure represents a kinetically optimized metastable state rather than the global equilibrium configuration. Maintaining this state through controlled processing is therefore crucial to preserving the alloy's exceptional combination of strength and ductility.

### 4.2. Deformation behavior in CRA alloy

The enrichment of Fe at LAGBs promotes deformation-induced martensitic transformation, thereby enhancing the alloy's ductility. It is well established that the SFE plays a critical role in controlling deformation mechanisms in metastable austenitic steels [54]. When the SFE of austenite falls below approximately 20 mJ/$m^2$, martensitic transformation becomes the dominant deformation behavior. For the CRA alloy, the calculated SFE at LAGBs is 27.5 mJ/$m^2$, which is close to this threshold. It should be noted that thermodynamic models may overestimate the SFE [55,56]. In addition to SFE, the driving force for martensitic transformation is crucial [57,58]. The tendency for austenite to undergo deformation-induced martensitic transformation increases with the ratio of driving force to SFE. We calculated the driving forces for martensitic transformation at both the LAGBs and in the matrix.

The expression proposed for the free energy difference between the BCC and FCC phases in the Fe-Ni system is used to calculate the free energy of FCC→BCC transformation ($\Delta G^{FCC\to BCC}(T)$) at *Ms* temperature.

$\Delta G^{FCC\to BCC}(T)$ for the binary solid solution of the Fe-Ni system can be written as follows [59]:

$$\Delta G^{FCC\to BCC} = (1-X_{Ni})\Delta G_{Fe}^{FCC\to BCC} + X_{Ni}\Delta G_{Ni}^{FCC\to BCC} + X_{Ni}(1-X_{Ni})E_{Fe-Ni}^{FCC\to BCC} \tag{6}$$

where $X_{Ni}$ is the mole fraction of the element Ni. $\Delta G_{Fe}^{FCC\to BCC}$ and $\Delta G_{Ni}^{FCC\to BCC}$ are the Gibbs free energy changes of the FCC→BCC transformation of elements Fe and Ni, respectively; $E_{Fe-Ni}^{FCC\to BCC}$ is the excess free energy coefficient for the binary system Fe-Ni. $\Delta G^{FCC\to BCC}(T)$ can be obtained by substituting the corresponding values of $\Delta G_{Fe}^{FCC\to BCC}$, $\Delta G_{Ni}^{FCC\to BCC}$ and $E_{Fe-Ni}^{FCC\to BCC}$ in Eq. (6) [60]:

$$\begin{aligned}\Delta G^{FCC\to BCC}(LAGBs) = (1-X_{Ni})\big(&\\ -1661.59-5.308T-1.69\times10^{-3}T^2+1.245T\ln(T)\big)&\\ +X_{Ni}\big(-15540+2.97\times10^{-3}T^2+1.64\times10^{-7}T^3\big)&\\ +X_{Ni}(1-X_{Ni})(15120+2.43T(1-\ln T)&\end{aligned} \tag{7}$$

$$\begin{aligned}\Delta G^{FCC\to BCC}(Matrix) = (1-X_{Ni})\big(&\\ -1590-6.55T-1.8\times10^{-3}T^2+1.43T\ln(T)\big)&\\ +X_{Ni}\big(&\\ -15540+2.97\times10^{-3}T^2+1.64\times10^{-7}T^3\big)&\\ +X_{Ni}(1-X_{Ni})(15120+2.43T(1-\ln T)&\end{aligned} \tag{8}$$

**Table 3**
Data concerning the FCC→HCP and FCC→BCC transformations in CRA alloy are studied.

| | Ms (°C) | $\Delta G^{FCC\rightarrow BCC}(Ms)$ (J/mol) | SFE (mJ/m$^2$) | $-\Delta G^{FCC\rightarrow BCC}/SFE$ ratio |
|---|---|---|---|---|
| LAGBs | 270.38 | −2413.07 | 27.5 | 87.75 |
| Matrix | 164.08 | −3155.22 | 54.5 | 57.89 |

The martensitic transition temperature (*Ms*) can be roughly estimated by the following empirical formula (9):

$$\mathrm{Ms}\ (^{\circ}\mathrm{C},\ \mathrm{at.}\ \%) = 545 - 71C + Al + 7Co - 14Cr - 15Cu - 23Mn - 8Mo - 6Nb - 13Ni - 4Si + 3Ti - 4V + 0W \quad (9)$$

The *Ms* of the LAGBs and matrix in CRA alloy are estimated as 270.38 °C and 164.08 °C, respectively.

The driving force/SFE ratio at the LAGBs exceeds that of the matrix (Table 3), indicating a greater propensity for martensitic transformation at the LAGBs. This observation aligns with EBSD results, which show that martensite first forms at the LAGBs. Furthermore, because the driving force for martensitic transformation in the matrix is also significant, the transformation occurring at the LAGBs can easily propagate and grow into the matrix. Our thermodynamic model, based on the average LAGB composition, captures the primary chemical driving force for martensitic transformation. The actual driving force is likely further enhanced by the local interfacial environment: the elastic strain field of the LAGBs may promote nucleation by accommodating the transformation strain, while the nanoscale chemical gradient provides additional compositional instability. The preferential martensite nucleation observed at these sites confirms that the composite driving force—integrating both chemical and mechanical factors—is maximized at Fe-enriched LAGBs. Thus, the enrichment of Fe at LAGBs reduces the austenite stability, promotes deformation-induced martensitic transformation, and ultimately enhances the alloy's strain-hardening capability and ductility.

While Calderon et al. demonstrated a thermally activated and reversible solvent (Au) segregation in Au–Pt alloys driven by differences in pure component grain boundary energies, our approach is based on a thermodynamically favorable and kinetically facilitated process, as confirmed by Thermo-Calc simulations showing a lower Gibbs free energy for the Fe-enriched state. This driving force is further enabled by cold rolling, which introduces dislocations serving as rapid diffusion pathways that stabilize Fe enrichment at LAGBs. This defect-mediated process is purposefully engineered to promote deformation-induced martensitic transformation, thereby achieving an unprecedented synergy of strength and ductility and extending the concept of solvent segregation into the realm of high-performance structural alloys.

Additionally, the pronounced yield plateau observed in the tensile response of the CRA alloy was further analyzed using digital image correlation to elucidate its physical origin (**Fig. S17**). Upon yielding at approximately 1.75 % strain, a well-defined Lüders band nucleates at an angle of ~ 45° to the tensile axis, initiating heterogeneous plastic deformation. As the strain increases to ~ 15 %, the band propagates steadily across the gauge length. Once the propagation is complete, the deformation mode transitions to uniform plastic flow throughout the specimen, which persists until the onset of diffuse necking and fracture. The Lüders band originates from the high initial density of immobile dislocations and LAGBs introduced during cold rolling, which require a critical stress for collective activation. The resulting localized plastic flow leads to an apparent yield drop and the formation of the plateau. Notably, the exceptional stability and extent of the plateau are not due to a lack of strain hardening, but rather to a dynamic balance between local softening and transformation-induced hardening. The intense strain concentration at the advancing band front provides a mechanical driving force that, together with Fe-enriched LAGBs of reduced stacking fault energy, promotes continuous transformation-induced plasticity (TRIP) activity. This transformation generates new phase boundaries and dislocations, providing sustained hardening that counterbalances the local softening associated with dislocation glide. The resulting dynamic equilibrium enables stable band propagation under nearly constant flow stress. The transition at ~ 15 % strain thus represents the completion of this propagation process and the onset of homogeneous deformation, during which accelerated TRIP activity governs the strong parabolic strain hardening observed in the CRA alloy.

Further insight into the deformation behavior of the CRA alloy is provided by its Kocks-Mecking (K-M) profile (work-hardening rate θ vs. true stress σ, Fig. 1**a, inset**), which reveals a distinct hardening profile diverging from the classical stages of FCC alloys [61]. This atypical profile can be delineated into three sequential regimes: In Stage I, at low stresses (< 1.75 GPa), the sharp decrease in work-hardening rate with increasing true stress reflects the predominantly elastic regime preceding macroscopic yielding. This is followed by Stage II, a regime of mild oscillations in work-hardening rate as the stress rises to ~ 2.0 GPa, corresponding to the nucleation and steady propagation of Lüders bands—a hallmark of materials exhibiting yield-point elongation [62]. Within these propagating bands, localized strain promotes the onset of strain-induced martensitic transformation, preferentially at LAGBs. Most critically, in Stage III, beyond a true stress of ~ 2.0 GPa, the K-M plot exhibits an unexpected upturn in the hardening rate ($d\theta/d\sigma > 0$), in contrast to the monotonic decrease characteristic of classical Stage III hardening in FCC metals [61]. This anomalous Stage III response reflects the rapid acceleration of the TRIP effect, driven by Fe-enriched LAGBs that facilitate martensitic transformation. The resulting increase in martensite fraction, confirmed by *in-situ* SXRD, introduces a high density of phase boundaries and dislocations, thereby sustaining a strong hardening rate and delaying the onset of necking. This transformation-assisted mechanism underpins the alloy's exceptional combination of strength and ductility.

In addition to deformation-induced martensitic transformation, the formation of extensive stacking faults during deformation in CRA alloy plays a role in enhancing ductility [63,64]. A high density of stacking faults reduces the dislocation mean free path, triggering the dynamic Hall-Petch effect, which further strengthens the alloy and improves ductility [65]. The effectiveness of these ductility-enhancing mechanisms is directly reflected in the fracture behavior. The presence of uniform dimples and the absence of grain-boundary facets in the fracture surface (**Fig. S18**) confirm a transgranular fracture mode, indicating that the solvent Fe-enriched LAGBs retain strong cohesion and do not act as crack initiation sites.

### 4.3. Strength contributions in CRA alloy

The CRA alloy demonstrates an impressive uniform elongation of 26.2 % and achieves a tensile yield strength of 1.74 GPa. Strength contributions from various mechanisms have been calculated. The yield strength of the CRA alloy is primarily composed of contributions from intrinsic strength ($\sigma_0$), solid solution strengthening ($\Delta\sigma_S$), grain boundary strengthening ($\Delta\sigma_G$), dislocation strengthening ($\Delta\sigma_D$) and

precipitation strengthening ($\Delta\sigma_P$). Thus, the overall yield strength $\sigma_y$ can be expressed as [66]:

$$\sigma_y = \sigma_0 + \Delta\sigma_S + \Delta\sigma_G + \Delta\sigma_D + \Delta\sigma_P \tag{10}$$

Intrinsic strength ($\sigma_0$) and solid solution strengthening ($\Delta\sigma_S$) are mainly attributed to lattice distortions arising from atomic size mismatches between the solute elements. The solid solution strengthening effect in the dilute solid solution alloys is typically described by the dilute solid solution model, which can be written as [40,67,68]:

$$\Delta\sigma_S = M\frac{G\cdot\varepsilon_S^{\frac{3}{2}}\cdot c^{\frac{1}{2}}}{700} \tag{11}$$

where $M$ is the Taylor coefficient, $G$ is the shear modulus, $c$ represents the total molar ratio of the solid solution elements, and $\varepsilon_S$ is the interaction parameter. Here, the constant 700 is an empirical proportionality factor that accounts for geometric and material-specific parameters in the interaction between dislocations and solute atoms. It follows the classical formulation for soft-obstacle solid-solution strengthening [69]. However, due to the complex composition of CRA alloy, the conventional dilute solid solution model is not directly applicable here [70]. As a result, we estimate the solid solution strength contribution to be 305 MPa, derived from experimental tensile data of the solid solution-treated ST alloy.

Grain boundary strengthening ($\Delta\sigma_G$) in CRA alloy is influenced by the presence of both low-angle grain boundaries and subgrain boundaries. The relationship between yield strength and grain size can be described by:

$$\sigma_0 + \Delta\sigma_G = \sigma_0 + k_y(2d)^{-n} \tag{12}$$

Thompson's research shows that for well-developed LAGBs, the value of $n$ can be taken as ranging from 1/2 to 1. In this study, we adopt $n$ = 1/2, which satisfies the Hall-Petch relationship [71,72]:

$$\Delta\sigma_G = k_y(2d)^{-1/2} \tag{13}$$

where $k_y = 226$ MPa/μm$^{1/2}$ is the Hall-Petch coefficient [73], $d = 0.317$ μm represents the average grain diameter measured by EBSD. The factor of 2 in $(2d)^{-1/2}$ denotes the effective spacing between geometrically necessary boundaries in cold-rolled structures, consistent with prior Hall–Petch treatments for deformed metals [74,75]. Based on this, the grain boundary strengthening contribution $\Delta\sigma_G$ is calculated to be approximately 284 MPa.

Dislocation strengthening ($\Delta\sigma_D$) in CRA alloy arises from the high dislocation density. Quantitative measurements of dislocation density were obtained through synchrotron X-ray diffraction, employing the Williamson-Hall method [76–78]. From the relationship:

$$\Delta K = \frac{0.9}{d} + \left(\frac{\pi N^2 b^2}{2}\right)^{\frac{1}{2}}\cdot\rho^{\frac{1}{2}}\cdot K\overline{C}^{\frac{1}{2}} + O\left(K^2\overline{C}\right) \tag{14}$$

where $d$ is the average grain size. $N$ is the Wilkens alignment parameter, which is determined by the effective outer cutoff radius $Re$ of the dislocations. The factor 0.9 is a standard constant used in dislocation line profile analysis, derived from the average dislocation contrast factor and the outer cutoff radius, as established in the classical works of Wilkens [76] and Ungár [79]. The value of $N$ is typically in the range of 1 to 2, and in this paper, it is taken as 1.2. $b = 0.254$ nm is the Burgers vector. $O$ stands for the higher-order term in the equation involving $K^2\overline{C}$ which can generally be ignored in this context. $h$, $k$, and $l$ are the Miller indices corresponding to each diffraction peak. $\Delta K$, $K$, and $\overline{C}$ are the full width at half-maximum (FWHM) of the diffraction peak, the diffraction vector, and the average contrast factor of the broadened peaks in reciprocal space, respectively. They are defined as follows:

$$\Delta K = \frac{\beta\cdot\cos\theta}{\lambda} \tag{15}$$

$$K = \frac{2\sin\theta}{\lambda} \tag{16}$$

$$\overline{C} = \overline{C}_{h00}\cdot\left(1 - q\cdot H^2\right) \tag{17}$$

$$H^2 = \left(h^2k^2 + k^2l^2 + l^2h^2\right)/\left(h^2 + k^2 + l^2\right) \tag{18}$$

where $\theta$ is the diffraction angle, $\beta$ is the full width at half maximum (FWHM) of the diffraction peak, and $\lambda$ is the X-ray wavelength (0.20738 nm). The parameter $\overline{C}_{h00}$ depends on the anisotropic elastic constants $C_{11}$, $C_{12}$, and $C_{44}$. The variable $q$ is a fitting parameter in X-ray diffraction line profile analysis. It quantifies the anisotropy of strain broadening, which is influenced by the crystal's elastic constants and the character of the dislocations (edge/screw ratio) [80,81]. To determine the dislocation density, the best linear fit of $\Delta K$ versus $K\overline{C}^{\frac{1}{2}}$ is performed according to Eq (14). As shown in **Fig. S19**, the slope of the fitted line is 0.02163, from which the dislocation density is determined to be 3.206 × $10^{15}$ m$^{-2}$. The dislocation density estimated using the Williamson-Hall method represents a volume-averaged value that includes both geometrically necessary dislocations associated with LAGBs and statistically stored dislocations within the matrix. Given that the CRA microstructure is dominated by a high density of LAGBs, this averaged density is considered representative of the overall defect state.

The dislocation strengthening ($\Delta\sigma_D$) is then calculated using the classical dislocation strengthening equation [40,82,83]:

$$\Delta\sigma_D = M\alpha Gb\rho^{\frac{1}{2}} \tag{19}$$

where $M$ is the Taylor coefficient, $\alpha$ is a constant that quantifies the intensity of dislocation interactions. A value of α ≈ 0.2 is typically employed for FCC alloys, as established in foundational studies of high-strength FCC systems [40], and $G$ is the shear modulus (81 GPa). This gives a dislocation strengthening contribution of approximately 704 MPa.

Precipitation strengthening ($\Delta\sigma_P$) is attributed to the presence of coherent nanoprecipitates in the CRA alloy. When the precipitates are sufficiently small and coherent, the shear mechanism governs the strengthening. Given the current morphology of the nanoprecipitates, dislocation shearing dominates the strengthening mechanism. Three factors contribute to the strengthening effect: particle-substrate coherence ($\Delta\sigma_{CS}$), modulus mismatch ($\Delta\sigma_{MS}$), and atomic ordering ($\Delta\sigma_{OS}$) [84–86]. The first two factors act before dislocation shearing, while the third becomes significant during shear. The overall strengthening contribution is determined by the largest of these sequential factors. The governing equations are as follows [87]:

$$\Delta\sigma_{CS} = M\cdot\alpha_\varepsilon(G\cdot\varepsilon)^{\frac{3}{2}}\left(\frac{rf}{0.5Gb}\right)^{\frac{1}{2}} \tag{20}$$

$$\Delta\sigma_{MS} = M\cdot 0.0055(\Delta G)^{\frac{3}{2}}\left(\frac{2f}{G}\right)^{\frac{1}{2}}\left(\frac{r}{b}\right)^{\frac{3m}{2}-1} \tag{21}$$

$$\Delta\sigma_{OS} = M\cdot 0.81\frac{\gamma_{APB}}{2b}\left(\frac{3\pi f}{8}\right)^{\frac{1}{2}} \tag{22}$$

Here, $\alpha_\varepsilon = 2.6$ (for FCC structures), $m = 0.85$, and $\varepsilon \approx \frac{2}{3}\cdot(\Delta a/a)$, where $\Delta a/a = 0.001573$, derived from synchrotron radiation measurements of lattice constants for the $L1_2$ precipitates and FCC matrix. The volume fraction of the precipitate phase ($f$) is 0.24. The shear modulus mismatch ($\Delta G$) between the precipitates and matrix is 4 GPa ($\Delta G = 81 - 77 =$ 4 GPa). The shear modulus ($G = 81$ GPa) and modulus mismatch ($\Delta G =$

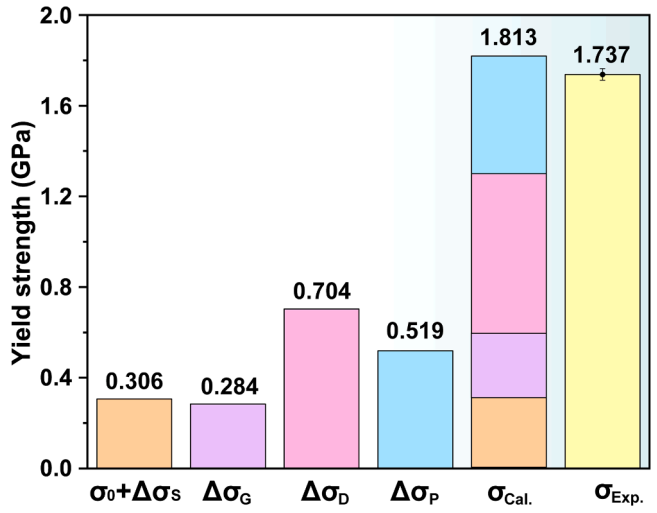


**Fig. 9. Strengthening contributions in CRA**. The summarized graphs illustrate the individual strengthening contributions in CRA. $\sigma_0$, $\Delta\sigma_S$, $\Delta\sigma_G$, $\Delta\sigma_D$ and $\Delta\sigma_P$ indicate intrinsic strengthening, solid solution strengthening, grain boundary strengthening, and precipitation strengthening, respectively. $\sigma_{Cal.}$ and $\sigma_{Exp.}$ represent the calculated and experimental yield strength, respectively. The calculated strengthening contributions are in good agreement with the experimental yield strength data.

4 GPa) used in the precipitation strengthening calculations were taken from literature for comparable Fe-Ni-Co based FCC systems [40], as the matrix chemistry in this work is compositionally analogous. The coefficient 0.81 is a standard empirical constant derived from the theoretical work of Brown and Ham and subsequent simulations by Foreman and Makin [88], representing the average interaction strength between a dislocation and a coherent precipitate. The antiphase boundary energy ($\gamma_{APB}$) is 200 mJ $m^{-2}$, based on $L1_2$ precipitates in Fe-Ni alloys [89]. Using these parameters, the contributions are calculated as $\Delta\sigma_{CS}$ = 71.48 MPa, $\Delta\sigma_{MS}$ = 24.287 MPa, $\Delta\sigma_{OS}$ = 519 MPa. As the atomic ordering term dominates, the total contribution of precipitation strengthening is determined to be 519 MPa. In the present model, the strengthening contribution is estimated using averaged parameters, which adequately capture the macroscopic behavior. However, a more advanced formulation could introduce a spatially dependent precipitate fraction to account for the gradient in strengthening near LAGBs. Such an approach would provide a more complete description of the hierarchical hardening architecture and is an important avenue for future investigation.

Coherent $L1_2$ nanoparticles with high density and volume fraction significantly enhance the alloy's strength, contributing 519 MPa to the yield strength. Synchrotron high-energy X-ray diffraction measurements reveal a dislocation density of $3.2 \times 10^{15}$ $m^{-2}$, which correlates with a strength contribution of 704 MPa. In contrast, the contributions from other mechanisms, including solid solution strengthening and grain boundary strengthening, are relatively minor (Fig. 9). Therefore, we attribute the exceptional yield strength of the CRA alloy primarily to precipitation strengthening and dislocation strengthening.

## 5. Conclusion

Here, we uncover an unprecedented phenomenon in a ferrous alloy, where Fe, the solvent element, preferentially segregates at low-angle grain boundaries (LAGBs), rather than the traditional solute elements. This Fe enrichment at LAGBs notably reduces the local stacking fault energy, inducing an austenite-to-martensite transformation upon deformation. The enhanced interface coherence between LAGBs and the matrix, together with a high density of coherent nanoprecipitates and dislocations, contributes to an exceptional combination of mechanical properties: an ultra-high yield strength of 1737 ± 39 MPa, achieved through synergistic precipitation and dislocation strengthening, alongside an exceptional uniform elongation of 26.2 % ± 3.1 %. Our findings challenge prevailing theories of element segregation and introduce transformative avenues for engineering alloys that combine extraordinary strength with high ductility.

The present results suggest that solvent enrichment at LAGBs can serve as a general design strategy to enhance ductility without compromising strength. By promoting defect-mediated segregation and exploiting thermodynamic driving forces, this approach may be applied to a wide range of multi-principal element alloys and brittle intermetallics. Future alloy design could leverage controlled processing routes to tailor solvent segregation at grain boundaries, enabling next-generation structural materials with optimized mechanical performance.

## CRediT authorship contribution statement

**Ting Liu:** Writing – original draft, Visualization, Methodology, Investigation, Formal analysis, Data curation. **Yunzhu Shi:** Writing – review & editing, Project administration, Funding acquisition, Conceptualization. **Liuliu Han:** Methodology, Formal analysis, Data curation. **Fei Zhang:** Formal analysis, Data curation. **Wei Chen:** Resources, Formal analysis, Data curation. **Hongyuan Wan:** Resources, Data curation. **Chao Ma:** Methodology, Formal analysis, Data curation. **Alexander Schökel:** Resources, Data curation. **Yan Ma:** Software, Resources, Data curation. **Shaolou Wei:** Resources, Formal analysis, Data curation. **Claudio Pistidda:** Software, Resources. **Zhifeng Lei:** Writing – review & editing, Writing – original draft, Supervision, Project administration, Funding acquisition, Conceptualization. **Zhaoping Lu:** Writing – review & editing, Supervision, Conceptualization.

## Declaration of competing interest

The authors declare that they have no known competing financial interests or personal relationships that could have appeared to influence the work reported in this paper.

## Acknowledgements

This research was funded by the National Natural Science Foundation of China (Nos. 52371153, 52471174), the Fundamental Research Funds for the Central Universities (Nos. 531118010621, 531118010671), and the National Natural Science Foundation of Hunan Province (No. 2025JJ30017). We acknowledge DESY (Hamburg, Germany), a member of the Helmholtz Association HGF, for the provision of experimental facilities. Parts of this research were carried out at the PETRA III beamline P02.1, and we would like to thank Dr. Alba San José Méndez for her assistance. Beamtime was allocated for proposals I-20230050 and I-20230183.

## Supplementary materials

Supplementary material associated with this article can be found, in the online version, at doi:10.1016/j.actamat.2025.121829.

## Data availability

The data supporting the findings of this study are available from the corresponding authors upon reasonable request.

## References

[1] M. Zhao, J.C. Brouwer, W.G. Sloof, A.J. Böttger, Surface segregation of ternary alloys: effect of the interaction between solute elements, Adv. Mater. Interfaces 7 (6) (2020) 1901784.

[2] M. Polak, L. Rubinovich, The interplay of surface segregation and atomic order in alloys, Surf. Sci. Rep. 38 (2000) 127–194.
[3] W. Zhang, X. Guo, J. Ren, J. Li, H. Xue, F. Tang, P. La, X. Lu, Double strengthening induced by grain boundary segregation of solute elements in gradient nano Ni-Co alloys, Phys. Chem. Chem. Phys. 25 (46) (2023) 32142–32150.
[4] M. Wagih, Y. Naunheim, T. Lei, C.A. Schuh, Grain boundary segregation predicted by quantum-accurate segregation spectra but not by classical models, Acta Mater. (2024) 119674.
[5] D. Wen, V. Tucker, M.S. Titus, A layer model for the kinetics of segregation in planar defects in multi-component materials, Acta Mater. 290 (2025) 120948.
[6] H. Pan, G. Qin, Y. Huang, Y. Ren, X. Sha, X. Han, Z.-Q. Liu, C. Li, X. Wu, H. Chen, C. He, L. Chai, Y. Wang, J.-f. Nie, Development of low-alloyed and rare-earth-free magnesium alloys having ultra-high strength, Acta Mater. 149 (2018) 350–363.
[7] Y. Su, Y. Wang, J. Shi, Microstructure and mechanical properties of laser DED produced crack-free Al 7075 alloy: effect of process parameters and heat treatment, Mater. Sci. Eng., A 857 (2022) 144075.
[8] H. Jia, R. Bjørge, L. Cao, H. Song, K. Marthinsen, Y. Li, Quantifying the grain boundary segregation strengthening induced by post-ECAP aging in an Al-5Cu alloy, Acta Mater 155 (2018) 199–213.
[9] J. Wang, R. Janisch, G.K.H. Madsen, R. Drautz, First-principles study of carbon segregation in bcc iron symmetrical tilt grain boundaries, Acta Mater. 115 (2016) 259–268.
[10] C.D. Barrett, A. Imandoust, H. El Kadiri, The effect of rare earth element segregation on grain boundary energy and mobility in magnesium and ensuing texture weakening, Scr. Mater. 146 (2018) 46–50.
[11] Y. Chen, N. Gao, G. Sha, S.P. Ringer, M.J. Starink, Microstructural evolution, strengthening and thermal stability of an ultrafine-grained Al-Cu-Mg alloy, Acta Mater. 109 (2016) 202–212.
[12] D. Raabe, S. Sandlöbes, J. Millán, D. Ponge, H. Assadi, M. Herbig, P.P. Choi, Segregation engineering enables nanoscale martensite to austenite phase transformation at grain boundaries: a pathway to ductile martensite, Acta Mater. 61 (16) (2013) 6132–6152.
[13] Y. Ma, B. Sun, A. Schökel, W. Song, D. Ponge, D. Raabe, W. Bleck, Phase boundary segregation-induced strengthening and discontinuous yielding in ultrafine-grained duplex medium-Mn steels, Acta Mater. 200 (2020) 389–403.
[14] G. Zhang, G. Chen, C. Panwisawas, X. Teng, Y. Ma, R. An, Y. Huang, J. Cao, X. Leng, First-principles study of oxygen segregation and its effect on the embrittlement of molybdenum symmetrical tilt grain boundaries, Acta Mater. 261 (2023) 119387.
[15] D. Zhao, O.M. Løvvik, K. Marthinsen, Y. Li, Segregation of Mg, Cu and their effects on the strength of Al Σ5 (210)[001]symmetrical tilt grain boundary, Acta Mater. 145 (2018) 235–246.
[16] S.-G. Park, K.-H. Lee, M.-C. Kim, B.-S. Lee, Effects of boundary characteristics on resistance to temper embrittlement and segregation behavior of Ni-Cr-Mo low alloy steel, Mater. Sci. Eng., A 561 (2013) 277–284.
[17] J.B. Seol, J.W. Bae, Z. Li, J. Chan Han, J.G. Kim, D. Raabe, H.S. Kim, Boron doped ultrastrong and ductile high-entropy alloys, Acta Mater. 151 (2018) 366–376.
[18] S. Calderon, W.-Y. Chen, M.S. Islam, S.S. Tripathy, M.P. de Boer, E.C. Dickey, G. S. Rohrer, A reversible solvent segregation transition at grain boundaries in gold-platinum alloys, Scr. Mater. 269 (2025) 116902.
[19] J. Petrazoller, J. Guénolé, S. Berbenni, T. Richeton, On the effect of elastic anisotropy and polarizability on solute segregation at low-angle grain boundaries, Comput. Mater. Sci. 249 (2025) 113642.
[20] C. Prescher, V.B. Prakapenka, DIOPTAS: a program for reduction of two-dimensional X-ray diffraction data and data exploration, High Pressure Res. 35 (3) (2015) 223–230.
[21] B.H. Toby, R.B. Von Dreele, GSAS-II: the genesis of a modern open-source all purpose crystallography software package, J. Appl. Crystallogr. 46 (2) (2013) 544–549.
[22] A.-C. Dippel, H.-P. Liermann, J.T. Delitz, P. Walter, H. Schulte-Schrepping, O. H. Seeck, H. Franz, Beamline P02.1 at PETRA III for high-resolution and high-energy powder diffraction, J. Synchrotron Radiat. 22 (3) (2015) 675–687.
[23] M. Basham, J. Filik, M.T. Wharmby, P.C.Y. Chang, B. El Kassaby, M. Gerring, J. Aishima, K. Levik, B.C.A. Pulford, I. Sikharulidze, D. Sneddon, M. Webber, S. S. Dhesi, F. Maccherozzi, O. Svensson, S. Brockhauser, G. Náray, A.W. Ashton, Data analysis WorkbeNch(DAWN), J. Synchrotron Radiat. 22 (3) (2015) 853–858.
[24] T. Kang, Z. Zhao, J. Liang, J. Guo, Y. Zhao, Effect of the austenitizing temperature on the microstructure evolution and mechanical properties of Q&P steel, Mater. Sci. Eng., A 771 (2020) 138584.
[25] L. Cho, E.J. Seo, B.C. De Cooman, Near-Ac3 austenitized ultra-fine-grained quenching and partitioning (Q&P) steel, Scr. Mater. 123 (2016) 69–72.
[26] K. Kim, S.-J. Lee, Effect of Ni addition on the mechanical behavior of quenching and partitioning (Q&P) steel, Mater. Sci. Eng., A 698 (2017) 183–190.
[27] Y. Wang, Y. Xu, R. Liu, F. Peng, X. Gu, T. Zhang, X. Hou, W. Sun, Microstructure evolution and mechanical behavior of a novel hot-galvanized Q&P steel subjected to high-temperature short-time overaging treatment, Mater. Sci. Eng., A 789 (2020) 139665.
[28] S. Yan, X. Liu, W.J. Liu, T. Liang, B. Zhang, L. Liu, Y. Zhao, Comparative study on microstructure and mechanical properties of a C-Mn-Si steel treated by quenching and partitioning (Q&P) processes after a full and intercritical austenitization, Mater. Sci. Eng., A 684 (2017) 261–269.
[29] L. Fan, T. Yang, Y. Zhao, J. Luan, G. Zhou, H. Wang, Z. Jiao, C.-T. Liu, Ultrahigh strength and ductility in newly developed materials with coherent nanolamellar architectures, Nat. Commun. 11 (1) (2020) 6240.
[30] S. Shin, C. Zhu, C. Zhang, K.S. Vecchio, Extraordinary strength-ductility synergy in a heterogeneous-structured β -Ti alloy through microstructural optimization, Mater. Res. Lett. 7 (11) (2019) 467–473.
[31] O. Bouaziz, D. Barbier, P. Cugy, G. Petigand, Effect of process parameters on a metallurgical route providing nano-structured single phase steel with high work-hardening, Adv. Eng. Mater. 14 (1–2) (2011) 49–51.
[32] B.-G. Zhang, X.-M. Zhang, H.-T. Liu, Microstructural evolution and mechanical properties of Ni-containing light-weight medium-Mn TRIP steel processed by intercritical annealing, Mater. Sci. Eng., A 793 (2020) 139289.
[33] W. Yu, L. Qian, X. Peng, T. Wang, K. Li, C. Wei, Z. Chen, F. Zhang, J. Meng, Roles of Al in enhancing the thermal stability of reverted austenite and mechanical properties of a medium-Mn TRIP steel containing 2.7 Mn, J. Mater. Sci. Technol. 167 (2023) 119–136.
[34] P. Shi, Y. Zhong, Y. Li, W. Ren, T. Zheng, Z. Shen, B. Yang, J. Peng, P. Hu, Y. Zhang, P.K. Liaw, Y. Zhu, Multistage work hardening assisted by multi-type twinning in ultrafine-grained heterostructural eutectic high-entropy alloys, Mater. Today 41 (2020) 62–71.
[35] J. Ren, M. Wu, C. Li, S. Guan, J. Dong, J.-B. Forien, T. Li, K.S. Shanks, D. Yu, Y. Chen, K. An, K.Y. Xie, W. Chen, T. Voisin, W. Chen, Deformation mechanisms in an additively manufactured dual-phase eutectic high-entropy alloy, Acta Mater. 257 (2023) 119179.
[36] J. Ren, Y. Zhang, D. Zhao, Y. Chen, S. Guan, Y. Liu, L. Liu, S. Peng, F. Kong, J. D. Poplawsky, G. Gao, T. Voisin, K. An, Y.M. Wang, K.Y. Xie, T. Zhu, W. Chen, Strong yet ductile nanolamellar high-entropy alloys by additive manufacturing, Nature 608 (7921) (2022) 62–68.
[37] Y. Lu, X. Wu, Z. Fu, Q. Yang, Y. Zhang, Q. Liu, T. Li, Y. Tian, H. Tan, Z. Li, T. Wang, T. Li, Ductile and ultrahigh-strength eutectic high-entropy alloys by large-volume 3D printing, J. Mater. Sci. Technol. 126 (2022) 15–21.
[38] S.L. Gibbons, R.A. Abrahams, M.W. Vaughan, R.E. Barber, R.C. Harris, R. Arroyave, I. Karaman, Microstructural refinement in an ultra-high strength martensitic steel via equal channel angular pressing, Mater. Sci. Eng., A 725 (2018) 57–64.
[39] M.W. Vaughan, P. Samimi, S.L. Gibbons, R.A. Abrahams, R.C. Harris, R.E. Barber, I. Karaman, Exploring performance limits of a new martensitic high strength steel by ausforming via equal channel angular pressing, Scr. Mater. 184 (2020) 63–69.
[40] J.Y. He, H. Wang, H.L. Huang, X.D. Xu, M.W. Chen, Y. Wu, X.J. Liu, T.G. Nieh, K. An, Z.P. Lu, A precipitation-hardened high-entropy alloy with outstanding tensile properties, Acta Mater. 102 (2016) 187–196.
[41] W.H. Liu, Z.P. Lu, J.Y. He, J.H. Luan, Z.J. Wang, B. Liu, Y. Liu, M.W. Chen, C.T. Liu, Ductile CoCrFeNiMox high entropy alloys strengthened by hard intermetallic phases, Acta Mater. 116 (2016) 332–342.
[42] Z. Lei, X. Liu, Y. Wu, H. Wang, S. Jiang, S. Wang, X. Hui, Y. Wu, B. Gault, P. Kontis, D. Raabe, L. Gu, Q. Zhang, H. Chen, H. Wang, J. Liu, K. An, Q. Zeng, T.G. Nieh, Z. Lu, Enhanced strength and ductility in a high-entropy alloy via ordered oxygen complexes, Nature 563 (7732) (2018) 546–550.
[43] Z. Zhang, P. Jiang, F. Yuan, X. Wu, Enhanced tensile properties by heterogeneous grain structures and coherent precipitates in a CoCrNi-based medium entropy alloy, Mater. Sci. Eng., A 832 (2022) 142400.
[44] W.-C. Chang, C.-H. Hsueh, Strengthening of CoCrNi medium entropy alloy with Ti additions, Intermetallics 163 (2023) 108072.
[45] J.X. Yan, J.Y. Qin, J.H. Liu, H. Chen, Y.H. Huang, M. Liu, C.H. Xia, F. Wang, X. D. Cui, J.B. Yang, Z.F. Zhang, Composition design study of strong and ductile Mo-alloyed CoCrNi medium-entropy alloys, J. Mater. Sci. Technol. 186 (2024) 37–47.
[46] H. Huang, J. Wang, H. Yang, S. Ji, H. Yu, Z. Liu, Strengthening CoCrNi medium-entropy alloy by tuning lattice defects, Scr. Mater. 188 (2020) 216–221.
[47] Y. He, J. Gao, Y. He, K. Shin, A new fcc-bcc orientation relationship observed in the strain-induced martensitic transformation of an austenitic stainless steel, Mater. Lett. 305 (2021) 130735.
[48] G.B. Olson, M. Cohen, A general mechanism of martensitic nucleation part II. FCC → BCC and other martensitic transformations, Metall. Trans. A 7A (1976) 1905–1914.
[49] P. Lejcek, Grain Boundary Segregation in Metals, Springer Science & Business Media, Berlin, Heidelberg, 2010.
[50] M.M. Gong, F. Liu, Y.Z. Chen, Modeling solute segregation in grain boundaries of binary substitutional alloys: effect of excess volume, J. Alloys Compd. 682 (2016) 89–97.
[51] L.T. Mushongera, M. Fleck, J. Kundin, Y. Wang, H. Emmerich, Effect of re on directional γ′-coarsening in commercial single crystal Ni-base superalloys: a phase field study, Acta Mater. 93 (2015) 60–72.
[52] Y.-C. Huang, Y.-C. Lai, Y.-H. Lin, S.-K. Wu, A study on the severely cold-rolled and annealed quaternary equiatomic derivatives from quinary HfNbTaTiZr refractory high entropy alloy, J. Alloys Compd. 855 (2021) 157404.
[53] G. N, C. T, Self-diffusion and Impurity Diffusion in Pure metals: Handbook of Experimental Data, Elsevier, 2008.
[54] O.G. ssel, L.K. ger, G. Frommeyer, L.W. Meyer, High strength Fe±Mn±(Al, Si) TRIP/TWIP steels development Ð properties Ð application, Int. J. Plast. 16 (2000) 1391–1409.
[55] P. Behjati, A. Najafizadeh, Role of chemical driving force in martensitic transformations of high-purity Fe-Cr-Ni alloys, Metall. Mater. Trans. A 42 (12) (2011) 3752–3760.
[56] S. Curtze, V.T. Kuokkala, A. Oikari, J. Talonen, H. Hänninen, Thermodynamic modeling of the stacking fault energy of austenitic steels, Acta Mater. 59 (3) (2011) 1068–1076.
[57] P. Behjati, A. Kermanpur, A. Najafizadeh, Application of martensitic transformation fundamentals to select appropriate alloys for grain refining through martensite thermomechanical treatment, Metall. Mater. Trans. A 44 (8) (2013) 3524–3531.

[58] M. Eskandari, A. Kermanpur, A. Najafizadeh, Formation of nanocrystalline structure in 301 stainless steel produced by martensite treatment, Metall. Mater. Trans. A 40 (9) (2009) 2241–2249.
[59] M. Moallemi, A. Kermanpur, A. Najafizadeh, A. Rezaee, H.S. Baghbadorani, P. D. Nezhadfar, Deformation-induced martensitic transformation in a 201 austenitic steel: the synergy of stacking fault energy and chemical driving force, Mater. Sci. Eng., A 653 (2016) 147–152.
[60] T.Y.H.X. ZUYAO, C. HONGBING, LUOSHOUFU, On thermodynamic calculation of ms and on driving force for martensitic transformations in Fe-C, J. Mater. Sci. 18 (1983) 3206–3212.
[61] U.F. Kocks, H. Mecking, Physics and phenomenology of strain hardening: the FCC case, Prog. Mater Sci. 48 (2003) 171–273.
[62] W. Mao, S. Gao, W. Gong, T. Kawasaki, T. Ito, S. Harjo, N. Tsuji, Martensitic transformation-governed Lüders deformation enables large ductility and late-stage strain hardening in ultrafine-grained austenitic stainless steel at low temperatures, Acta Mater. 278 (2024) 120233.
[63] S.Q. Zhu, S.P. Ringer, On the role of twinning and stacking faults on the crystal plasticity and grain refinement in magnesium alloys, Acta Mater. 144 (2018) 365–375.
[64] Z. Chen, C. Lu, Y. Zhuo, Z. Xia, X. Zhu, C. Wang, Q. Jia, Ductility enhancement of additively manufactured CoCrMo alloy via residual stress tailored high stacking fault probability, Scr. Mater. 235 (2023) 115626.
[65] Z. Zhang, L. Xu, G. Qin, Y. Ma, X. Wu, F. Yuan, Superior tensile properties at cryogenic temperature induced by dual-graded structures in medium entropy alloys, Mater. Des. 244 (2024) 113101.
[66] W. Li, T.-H. Chou, T. Yang, W.-S. Chuang, J.C. Huang, J. Luan, X. Zhang, X. Huo, H. Kong, Q. He, X. Du, C.-T. Liu, F.-R. Chen, Design of ultrastrong but ductile medium-entropy alloy with controlled precipitations and heterogeneous grain structures, Appl. Mater. Today 23 (2021) 101037.
[67] C.A. Schuh, T.G. Nieh, H. Iwasaki, The effect of solid solution W additions on the mechanical properties of nanocrystalline Ni, Acta Mater. 51 (2) (2003) 431–443.
[68] J.Y. He, W.H. Liu, H. Wang, Y. Wu, X.J. Liu, T.G. Nieh, Z.P. Lu, Effects of Al addition on structural evolution and tensile properties of the FeCoNiCrMn high-entropy alloy system, Acta Mater. 62 (2014) 105–113.
[69] T.H. Courtney, Mechanical Behavior of Materials, Waveland Press, Long Grove, IL, 2000.
[70] C.R. LaRosa, M. Shih, C. Varvenne, M. Ghazisaeidi, Solid solution strengthening theories of high-entropy alloys, Mater. Charact. 151 (2019) 310–317.
[71] A.W. Thompson, Substructure strengthening mechanisms, Metall. Mater. Trans. A 8 (1977) 833–842.
[72] U.F. Kocksa, H. Mecking, Physics and phenomenology of strain hardening: the FCC case, Prog. Mater. Sci. 48 (2003) 171–273.
[73] W. Liu, H. Tu, M. Gao, X. Su, S. Zhang, C. Huo, H. Yang, High performance DLC/BP and ZnS/YbF3 double-layer protective and antireflective coatings, J. Alloys Compd. 581 (2013) 526–529.
[74] X. Huang, S. Morito, N. Hansen, T. Maki, Ultrafine structure and high strength in cold-rolled martensite, Metall. Mater. Trans. A 43 (10) (2012) 3517–3531.
[75] B.L. Li, A. Godfrey, Q.C. Meng, Q. Liu, N. Hansen, Microstructural evolution of IF-steel during cold rolling, Acta Mater. 52 (4) (2004) 1069–1081.
[76] M. Wilkens, The determination of density and distribution of dislocations in deformed single crystals from broadened X-ray diffraction profiles, Phys. Status Solidi A 2 (2) (1970) 359–370.
[77] T. Ungár, Characterization of nanocrystalline materials by X-ray line profile analysis, J. Mater. Sci. 42 (5) (2006) 1584–1593.
[78] T.U. R, S. OTT, P.G. SANDERS, A.B. LY, J.R. WEERTMAN, Dislocations, grain size and planar faults in nanostructured copper determined by high resolution X-ray diffraction and a new procedure of peak profile analysis, Acta Mater. 46 (1998) 3693–3699.
[79] T. Ungár, Dislocation densities, arrangements and character from X-ray diffraction experiments, Mater. Sci. Eng., A 309 (2001) 14–22.
[80] M. Wang, M.X. Huang, Abnormal TRIP effect on the work hardening behavior of a quenching and partitioning steel at high strain rate, Acta Mater. 188 (2020) 551–559.
[81] T.U. r, I. Dragomir, A... ReÂveÂsz, A. BorbeÂly, The contrast factors of dislocations in cubic crystals: the dislocation model of strain anisotropy in practice, J. Appl. Crystallogr. 32 (1999) 992–1002.
[82] J. Su, D. Raabe, Z. Li, Hierarchical microstructure design to tune the mechanical behavior of an interstitial TRIP-TWIP high-entropy alloy, Acta Mater. 163 (2019) 40–54.
[83] G. Laplanche, A. Kostka, O.M. Horst, G. Eggeler, E.P. George, Microstructure evolution and critical stress for twinning in the CrMnFeCoNi high-entropy alloy, Acta Mater. 118 (2016) 152–163.
[84] H. Wen, T.D. Topping, D. Isheim, D.N. Seidman, E.J. Lavernia, Strengthening mechanisms in a high-strength bulk nanostructured Cu-Zn-Al alloy processed via cryomilling and spark plasma sintering, Acta Mater. 61 (8) (2013) 2769–2782.
[85] K. Ma, H. Wen, T. Hu, T.D. Topping, D. Isheim, D.N. Seidman, E.J. Lavernia, J. M. Schoenung, Mechanical behavior and strengthening mechanisms in ultrafine grain precipitation-strengthened aluminum alloy, Acta Mater. 62 (2014) 141–155.
[86] D.N. Seidman, E.A. Marquis, D.C. Dunand, Precipitation strengthening at ambient and elevated temperatures of heat-treatable Al(Sc) alloys, Acta Mater 50 (2002) 4021–4035.
[87] C. Booth-Morrison, D.C. Dunand, D.N. Seidman, Coarsening resistance at 400 °C of precipitation-strengthened Al-Zr-Sc-Er alloys, Acta Mater. 59 (18) (2011) 7029–7042.
[88] A.J. Ardell, Precipitation hardening, Metall. Trans. A 16A (1985) 2131–2165.
[89] Y. Yang, T. Chen, L. Tan, J.D. Poplawsky, K. An, Y. Wang, G.D. Samolyuk, K. Littrell, A.R. Lupini, A. Borisevich, E.P. George, Bifunctional nanoprecipitates strengthen and ductilize a medium-entropy alloy, Nature 595 (7866) (2021) 245–249.